AD_____

Award Number: DAMD17-99-1-9122

TITLE: A Method for Simulating Mammograms

PRINCIPAL INVESTIGATOR: Robert M. Nishikawa, Ph.D.

CONTRACTING ORGANIZATION: The University of Chicago
                            Chicago, Illinois   60637

REPORT DATE: August 2004

TYPE OF REPORT: Final Addendum

PREPARED FOR: U.S. Army Medical Research and Materiel Command
                Fort Detrick, Maryland   21702-5012

20050630 048

REPORT DOCUMENTATION PAGE

Public reporting burden for this collection of information is estimated to average 1 hour per response, including the time for reviewing instructions, searching existing data sources, gathering and maintaining the data needed, and completing and reviewing this collection of information. Send comments regarding this burden estimate or any other aspect of this collection of information, including suggestions for reducing this burden to Washington Headquarters Services, Directorate for Information Operations and Reports, 1215 Jefferson Davis Highway, Suite 1204, Arlington, VA 22202-4302, and to the Office of Management and Budget, Paperwork Reduction Project (0704-0188), Washington, DC 20503

1. AGENCY USE ONLY (Leave blank)	2. REPORT DATE August 2004	3. REPORT TYPE AND DATES COVERED Final Addendum (1 Aug 2003 - 31 Jul 2004)

4. TITLE AND SUBTITLE	5. FUNDING NUMBERS
A Method for Simulating Mammograms	DAMD17-99-1-9122

6. AUTHOR(S)
Robert M. Nishikawa, Ph.D.

7. PERFORMING ORGANIZATION NAME(S) AND ADDRESS(ES)	8. PERFORMING ORGANIZATION REPORT NUMBER
The University of Chicago Chicago, Illinois 60637 E-Mail: r-nishikawa@uchicago.edu	

9. SPONSORING / MONITORING AGENCY NAME(S) AND ADDRESS(ES)	10. SPONSORING / MONITORING AGENCY REPORT NUMBER
U.S. Army Medical Research and Materiel Command Fort Detrick, Maryland 21702-5012	

11. SUPPLEMENTARY NOTES

12a. DISTRIBUTION / AVAILABILITY STATEMENT	12b. DISTRIBUTION CODE
Approved for Public Release; Distribution Unlimited	

13. ABSTRACT (Maximum 200 Words)

This project is to facilitate research in digital mammography, in particular computer-aided diagnosis (CAD). A major limitation to the rapid development and subsequent clinical implementation of CAD is the lack of mammograms with absolute truth information. We are developing a method to produce simulated mammograms with known truth. The method relies on a model of image formation that takes into account the absorption of x-rays in the phosphor, subsequent conversion to light and the scattering of the light within the phosphor. The model also takes into account the finite thickness of the phosphor, the divergence of the x-ray beam, k-fluorescence radiation, and noise due to film granularity and from the film digitizer. We compared the simulated measurements and images with measurements from actual systems and real images. The resolution and noise properties of the simulated image closely match that of a real image, but certain aspects of the noise model need to be improved. By using more realistic modeling, we have found that k-fluorescence reabsorption can reduce the noise power spectrum by a factor of 70% compared to 20% in previous analyses. Incorporation of this new finding will allow for simulations that are more realistic.

14. SUBJECT TERMS		15. NUMBER OF PAGES
Breast cancer, mammography, modeling, computer simulation		97
		16. PRICE CODE

17. SECURITY CLASSIFICATION OF REPORT	18. SECURITY CLASSIFICATION OF THIS PAGE	19. SECURITY CLASSIFICATION OF ABSTRACT	20. LIMITATION OF ABSTRACT
Unclassified	Unclassified	Unclassified	Unlimited

Table of Contents

4. INTRODUCTION

This project is to facilitate research in digital mammography and related technologies, in particular computer-aided diagnosis (CAD) and image processing. A major limitation to the rapid development and subsequent clinical implementation of these technologies is the lack of a standardized set of mammograms with absolute truth (e.g., exact location and extend of a cancer) to be used in development and evaluation. We are developing a method to produce computer-simulated mammograms. The approach is to model the creation of the mammogram on the computer -- all steps from x rays exiting the breast to the image being displayed on a light box. The basic model, which we have developed previously, has been improved and is combined with accurate information of the appearance of normal breast anatomy and of benign and malignant breast lesions. These are obtained from high quality images of cadaver breasts and biopsy specimens. Our approach is similar to that of Van Metter *et al.* who modeled chest radiographs [Van Metter 1986]. We believe that this technique can produce simulated mammograms that appear to be actual mammograms. This hypothesis is being tested by performing quantitative comparisons of simulated and real mammograms.

5.   BODY OF REPORT

5.1 Tasks

We originally proposed four tasks in the Statement of Work, which are listed below. Not all the tasks were completed and some of the tasks were modified.

1. To obtain radiographs of mastectomy and tissue specimens:

(a) radiograph 100 different mastectomy breast tissues at 2.0 times geometric magnification recording image on direct film (without intensifying screen) at five different orientations;

(b) radiograph 240 different tissue specimens at 4.0 times geometric magnification recording images on direct film (without intensifying screen) at five different orientations; and

(c) segment lesions from specimen radiographs and measure their size, contrast, and shape metrics.

2. To develop further a computer model of image formation:

(a) modify previously developed model for point source versus parallel beam;

(b) measure and model detector noise for film digitizer and screen-film system;

(c) measure scatter as a function of position in the image; and

(d) measure beam intensity as a function of position in the image.

3. To produce simulated mammograms:

(a) produce simulated mammograms with and without lesions;

4

(b) make preliminary comparison to actual mammograms; and

(c) make adjustments to model, if necessary.

4. To evaluate simulated images:

(a) collect real mammograms: normals and those with lesions;

(b) compare real and simulated mammograms based on quantitative measurements;

(c) conduct pilot observer study; and

(d) conduct observer study comparing ROIs from real and simulated mammograms.

5.1.1 Obtain radiographs of tissue specimens and mastectomies

We partially completed tasks (a) and (c), but we did not start (b). We have decided to use cadaver breasts instead of mastectomy specimens, because they are easier to obtain. We have fourteen cadaver breasts that have been imaged using plain film. We have not yet collected specimen radiographs. Figure 1 shows an example of a piece of a cadaver breast.

5.1.2 Further development of computer simulation method

The theoretical basis for the model has been developed previously by the PI, but with a number of simplifying assumptions [Nishikawa 1989, 1990a, b]. For this project, we need to check these assumptions and include other relevant factors particular to our application. In
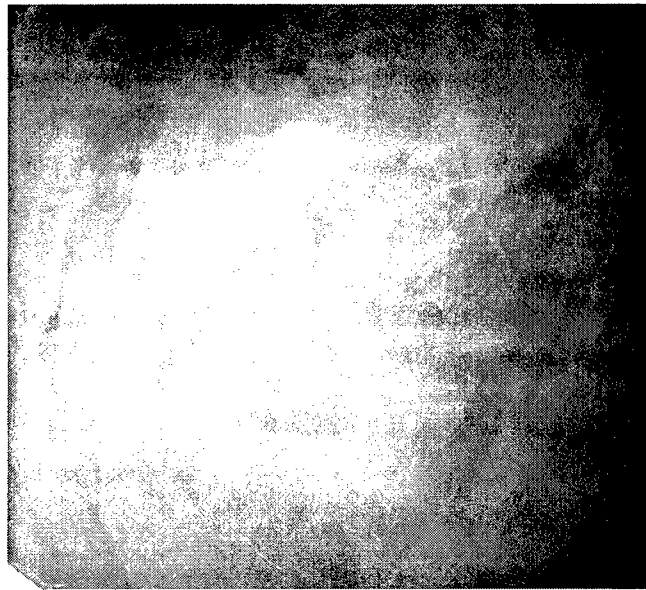
Figure 1. A portion of a screen-film image of a cadaver breast. Cadaver breasts are imaged with high fidelity (film only, no screen, using a high x-ray exposure and geometric magnification). Those images are digitized at 50 microns and used as input to our simulation model. Folds in the skin are apparent in the image and can be removed by placing the breast in saline.

5

addition, we need to covert the theory into a computer program that can produce a simulated image. Our efforts in these areas are described below.

We originally planned to modify our model to account for scattered radiation and non-uniformity of the x-ray beam. We still plan to incorporate these modifications, as they are fairly straightforward to implement. However, instead of working on these modifications, we chose instead to incorporate k-fluorescence re-absorption into our model as this is not straightforward and greatly expands the usefulness of our model. At the time of submission of our proposal, GdO_2S_2 was the dominant phosphor in use for mammography, both screen-film systems and experimental (full-field) and commercial (small-field) digital systems. The k-edge of this phosphor is well above the energies used in mammography, so k-fluorescence will not occur. However, the dominant phosphors in digital systems today are CsI and selenium. CsI has a k-edge at approximately 33 and 36 keV and selenium at approximately 13 keV. These energies are important for digital mammography, where x-ray beams as high as 40 kVp are used in commercial systems. Therefore, to be accurate, k-fluorescence re-absorption needs to be incorporated into our model.

5.1.2.a. Modify model from parallel beam of x rays to x rays from a point source.

In our previous model, we assumed that the x rays incident on the detector were at normal incidence (parallel beam). In practice, most x rays are incident at angles slightly less than 90 degrees. As illustrated in Fig. 2, x rays originating from a focal spot a finite distance from the detector will produce an x-ray beam that is diverging and is incident on the detector at some angle defined by θ, where θ depends on the distance of the focal spot from the detector, and the x-y position of the x ray incident on the detector – the larger the x-y position, the larger the angle. If the x rays are parallel and are incident at 90 degrees to the detector, then each pixel at the output has a one-to-one correspondence to a point at the input, in terms of energy deposition (ignoring scattered x rays). If the beam diverges however, depending on the depth of interaction of the x ray in the detector, a pixel at the output can have contributions from x rays that entered the detector at several different points at the input surface. In other words, the position of where the x ray would actually interact will be different from the position calculated by the model and this difference is Δ.

We have calculated the difference in energy deposition in the detector assuming a parallel beam and a diverging x-ray beam. Standard patient geometry is a focal-film distance of 65 cm and maximum detector size of 24x30 cm, with the central axis of the beam at one edge of the detector, centered in the other direction). Then assuming a phosphor thickness of 85 microns, we have calculated that the maximum energy spread because of a diverging beam is 35 microns (i.e., the difference between parallel and non-parallel beam assumptions is a 35-micron difference in the point at which the x ray is absorbed). This will occur at the periphery of the detector and only for those x rays interacting in the bottom of the phosphor (i.e., furthest from the source).

6
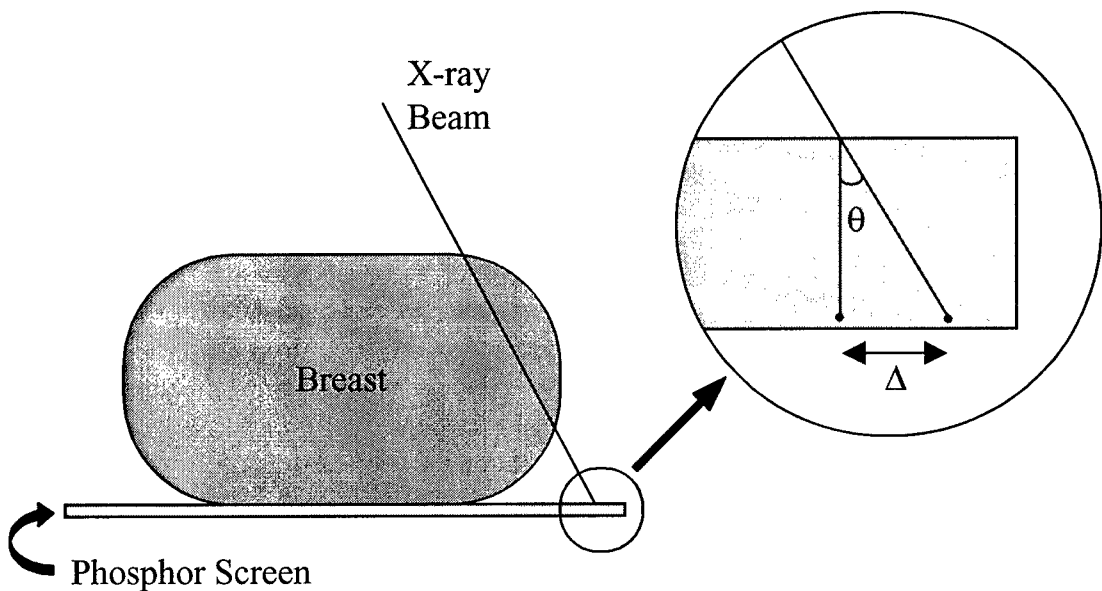
Figure 2. A schematic representation of the geometry of the x-beam incident on the phosphor screen as seen from a coronal view. The x-ray beam originates from a focal spot that is 65 cm above the screen. As a result, most x rays are incident on the detector at some angle θ>0. In our model, we assume that the x rays are incident at θ=0 degrees (normal incidence) as if they were a parallel beam of x-rays. This can produce a discrepancy (Δ) between where the x ray actually interacts in the screen and where it interacts according to our model. The value of Δ depends on the depth at which the x ray interacts and θ, which depends on the x-y position of the incident x ray. Note that the compression plate is not shown and that the angle depicted has been exaggerated to illustrate the point.

Figure 3 shows the fraction of x rays entering the phosphor at a given x-y location that will interact in the screen more than 17 microns laterally from the point it entered the screen. That is, this figure shows the fraction of x-ray interactions that will give rise to more than a 17-micron error when assuming all x-rays enter the screen at right angles compared to the real situation where the x rays enter the screen at some angle slightly less than 90 degrees. For this calculation, it is assumed that the x rays originate from a point source 65 cm above the page, centered at 0,0. For example, a 17-micron difference will occur at the very farthest corner of the screen for less than 40% of all x-ray interactions at that point. The average size compressed breast is approximately 100 cm^2. Therefore, for most breasts the difference between a parallel beam of x rays and a diverging beam is negligible. For larger breasts, the difference is minimal.

Since we will initially use a 17-micron pixel size at the output to form the image, and subsequently form larger pixels by averaging, we need to take the beam divergence into account to be absolutely accurate. However, only 12.5% of all interactions in the screen will lead to a small error and most if not all of these will be for pixels outside of the breast area. Because of the added complexity a non-parallel beam introduces, we have initially assumed a parallel beam in our calculations. If we find that this assumption produces poor results, we will modify our calculations for a diverging beam.
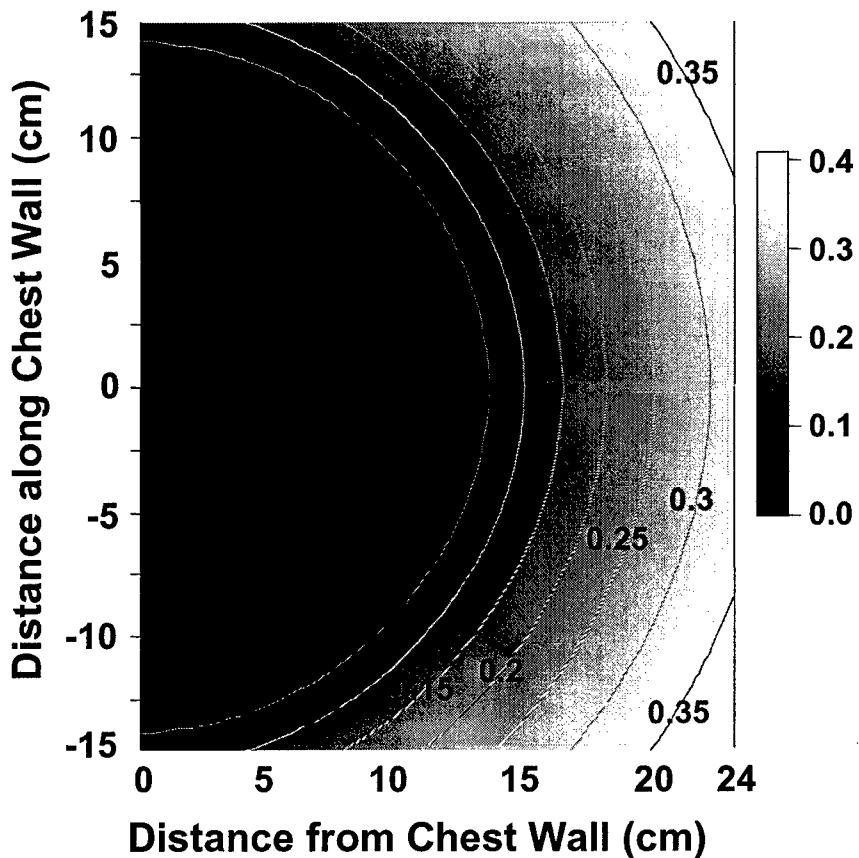
Figure 3. This iso-plot shows the fraction of x-rays that interact within a phosphor screen for which there is a 17-micron difference between two x-rays beams entering the phosphor at the same location one at normal incidence and one at angle. The x rays are assumed to have originated from a point 65 cm above the surface of the screen directly above the (0,0) point of the screen and the screen is 85-microns thick. The typical screen-film system used in mammography is 18x24 cm. For larger breasts, a 24x30 cm system is used. The inner contour covers an area of 265 cm^2, which is more than twice the size of an average compressed breast.

Note that the image is still formed using a diverging beam, so that the appearance of the tissue is correct. It is only once that the x rays impinge on the screen that we assume that they enter the screen at normal incidence, even though they may have arrived at the screen at not normal incidence.

5.1.2.b. Model detector noise for film digitizer and screen-film system.

Based on published noise power spectra of film [Bunch 1999] we integrated the spectra, weighted by the Fourier spectrum of a 50-micron scanning aperture. This gives us the standard deviation (square root of the integral) as a function of film density (see Figure 4). This was done for different film optical densities. Then assuming the noise on the film follows Gaussian statistics, we used a random number generator to produce a noise pattern that is added to the simulated image. That is, given a pixel with a certain film density, we generate a random number

8
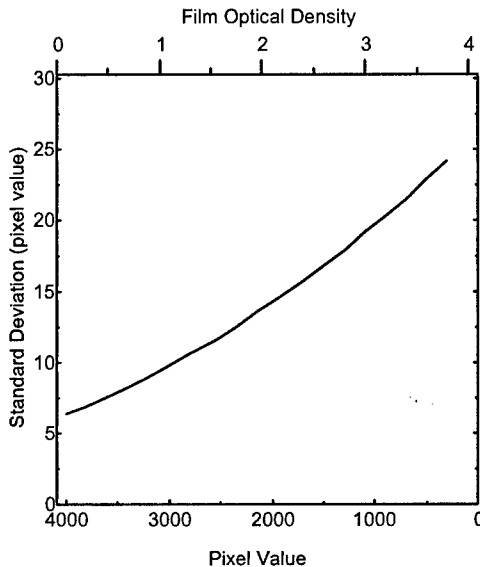
Figure 4. The relationship between the noise for a 50-micron pixel (as given by the standard deviation) as a function of the film optical density. This gives the magnitude of the noise due to film granularity.

that is from a Gaussian distribution with zero mean and a standard deviation corresponding to that film density, and then add this number to the pixel value.

We have also data on the noise of the film digitizer as a function of film density that we have measured in our laboratory (see Figure 5). To obtain these data, we digitized a calibration strip that had near-noiseless squares of constant optical densities from 0.10 to 4.0. Again, assuming Gaussian statistics, a random number generator is used to produce a noise pattern that is added to the simulated image. This information is necessary because we are using digital data for our comparison (simulated versus real) observer study, so we need to model digitization noise. We are using digital data because, if we printed the simulated images on film and used film for comparison, it would be obvious which images were simulated because they would look pixilated. Note that compare to film granularity noise, the noise due to the digitizer is insignificant under most conditions. However, at film densities above approximately 3.0, the two noise sources are comparable.

5.1.2.c. Measure scatter as a function of position in the image

Our original plan was to measure the scatter as a function of position in the image by placing lead blockers under the excised breast specimen. This would allow us to calculate the scatter to primary ratio at several points in the breast. Then by interpolation, we could estimate the scatter field for the whole breast. This scatter field would then be added to the simulated image. The drawback of this method is that we would need to repeat the experiment for every breast specimen that we would be simulating and the result would not necessarily be accurate, because of uncertainties in interpolation.

9
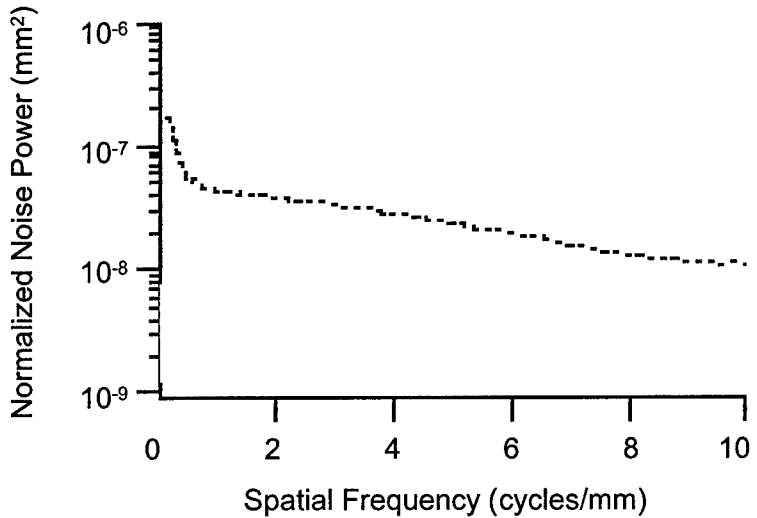
Figure 5. The noise power spectrum of the film digitizer for a film with an optical density of 1.5.

Instead, we will incorporate scatter into our model using a scatter term based on measured point-spread functions for scatter measured by Boone *et al.* [Boone 2002]. For each pixel at the output of the detector, the number of x rays interacting in a column through the detector is computed. That is, at the output of the phosphor, there is an image corresponding to the number of x rays interacting in the phosphor at each pixel. We will convolve this with the point-spread function for scatter, which is dependent on the breast thickness and very weakly on the energy of the x-ray beam. Figure 6 shows a point-spread function of scatter for a 30-kVp beam and a 6-cm thick breast.

We have not yet incorporated scatter into our model, as we are working on the noise aspects of the model first. It will.be straightforward to implement because we only need to perform a convolution. This will be done in the spatial frequency domain as a multiplication by taking the Fourier transform of the scatter point-spread function and the image at the output of the detector. We already perform some of the calculations of the model in the spatial frequency domain, so the image is already in the spatial frequency domain. We do not anticipate any difficulty implementing this correction.

5.1.2.d. Measure beam intensity as a function of position in the image

The intensity distribution of x rays from the Faxitron does not match that of a standard x-ray machine. Therefore, to more accurately simulate mammograms this difference needs to be corrected. This is done by multiplying the input image to our simulation program by the ratio of the x-ray intensity of a mammography machine to the x-ray intensity of the Faxitron. We have measured the x-ray intensity of the Faxitron, but we haven't measure the intensity on a mammography system, yet. Since we are only simulating limited sized areas within a mammogram, this correction is a second order one. Further, at this stage we are only comparing

10
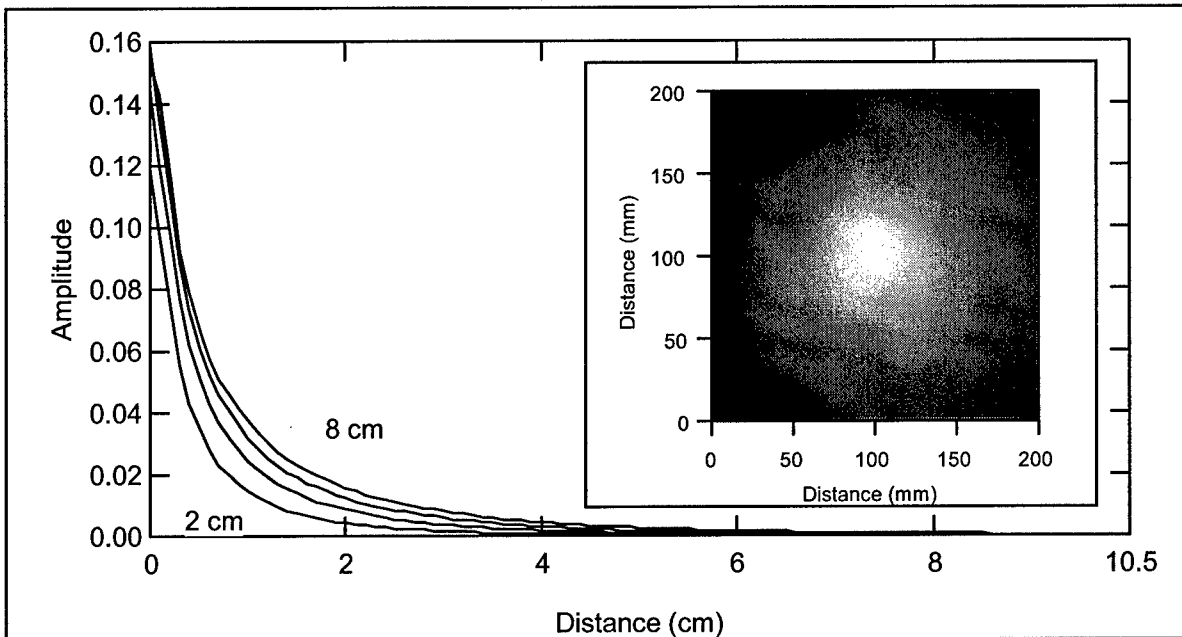
Figure 6. The point-spread function due to scattered radiation within the patient for compressed breast thicknesses ranging from 2 cm to 8 cm. The inset shows the 2D distribution of the point spread function for a 6-cm compressed breast. The data are for a 30 kVp mammographic spectrum, although the point spread functions are nearly independent of kVp.

images taken on the Faxitron. We do not anticipate any difficulty implementing this correction in the future.

5.1.2.e. K-fluorescence re-absorption (research beyond original statement of work)

Many x-ray detectors use a phosphor screen to convert the x-ray quanta into visible light photons that are subsequently collected by an optical detector. Fluorescent x rays can be produced within the phosphor. Some of these fluorescent x-ray quanta are reabsorbed in the phosphor. This fluorescent x-ray re-absorption affects the quality of images. We have developed a 3D convolution model to numerically simulate the characteristic x-ray re-absorption inside an image detector or intensifying screen with Monte Carlo technology. The 3D model is built through analyzing the physic process of creation, traveling, and absorption of characteristic x-ray quanta so that it can simulate the noise properties of characteristic x-ray re-absorption accurately. The phosphor layer of an image detector is conceptually divided into multiple sub-layers and every sub-layer is conceptually divided into multiple voxels based on the pixel size of a digital image. The 3D model computes the number distribution of reabsorbed characteristic x-ray quanta in every sub-layer using a pre-calculated convolution kernel. The convolution kernel gives the probability distribution that a characteristic x-ray quantum can be reabsorbed by a voxel. A cut-off window of the convolution is calculated to reduce the computation time. This 3D convolution model shows that most characteristic x-ray re-absorption blurs the image. However, some of characteristic x-ray re-absorption enhances the primary x-ray input, depending on the relative position between the creation site and re-absorption site of the fluorescent x rays. The simulation result is used to quantitatively analyze the effect of the fluorescent x-ray re-

11

absorption on the imaging performance of the detector or intensifying screen. The calculation to a cesium iodide layer with pixel size 17x17 microns shows that the characteristic re-absorption may reduce the modulation transfer function of the image detector as much as 10% at some spatial frequency, which is close to the measurement. It also reduces the NPS at non-zero spatial frequencies.

The details of the method are given in a preprint, which is attached to this report. We also develop one new scientific finding in this work. We have demonstrated that the depth within the phosphor at which the fluorescent x-ray is re-absorbed affects image quality. Metz and Vyborny previously showed theoretically that the effect on the NPS of the re-absorption is to decrease the NPS at high spatial frequencies by a constant amount [Metz 1983]. This work has been confirmed, again theoretically using different methods, by Hillen et al. [Hillen 1991] and Yao and Cunningham [Yao 2001]. In the theoretical models used to date, it is assumed that the phosphor screen is one slab of phosphor. In our work, we assume the phosphor is made of a stack of many thin layers of phosphor. The affect this has on the NPS is shown in Fig. 7. The results show that when the screen is properly modeled the reduction in the NPS at high spatial frequency is much more dramatic. In the single slab model, the reduction is 20%. When the screen is modeled as many thin slabs, our results show that the reduction is 70%.
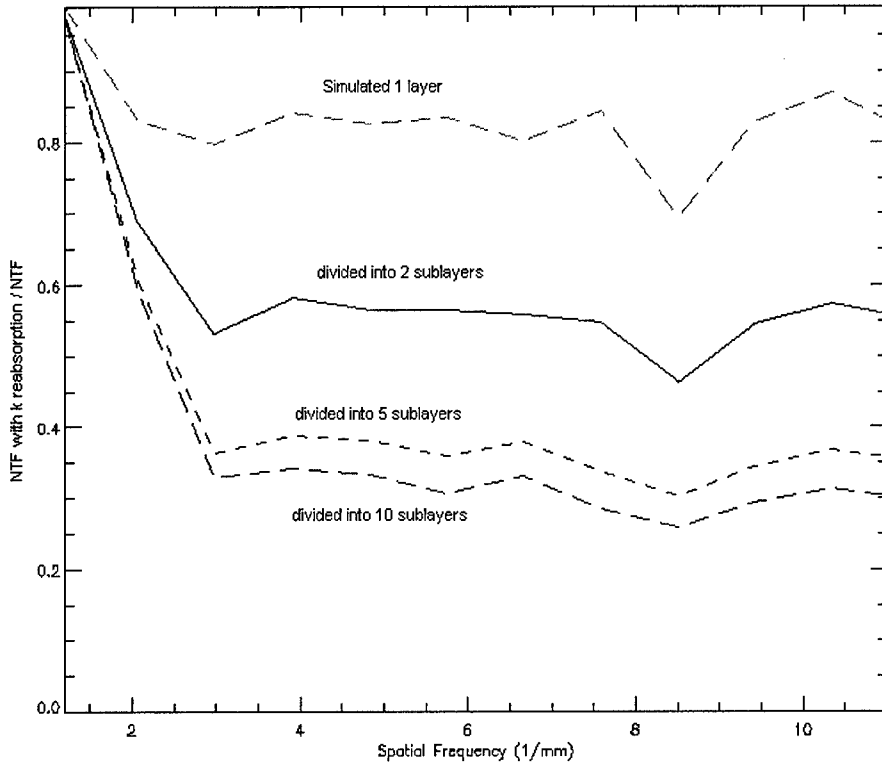

Figure 7. This shows the ratio of the shape of the noise power spectrum (NTF) when the effect of K-fluorescence is modeled to when it is not. The different curves show the effect of the depth within the phosphor that the K-fluorescence is reabsorbed. As the screen is considered to be composed of more layers, the ratio decreases at high spatial frequencies. Previous work in this area considered the screen to be a single thick slab, resulting in an underestimate of the effect of k-fluorescence reabsorption on the noise power spectrum. The curves were generated by using a Monte Carlo model.

5.1.3. Produce simulated mammogram

We have tested our simulation technique using phantoms and standard image quality metrics: modulation transfer function (MTF) and noise power spectrum (NPS). Since images will be made on the Kodak Min-R 2000 screen-film system, we have compared the characteristics of our simulated images with those for the Min-R 2000 system, based on published data.

To examine the resolution properties of our simulated image, we simulated a point source of x rays (see Fig. 8) and used it to calculate the modulation transfer function (MTF) (see Fig. 9). The MTF from the simulated image and published MTF [Bunch 1999] show excellent agreement – better than 5%.

To examine the noise properties of our simulated image, we generated a uniform random noise image using a Gaussian random number generator (see Figure 10). The output image from our simulation model is then used to calculate the NPS. Currently, we do not have accurate information of the conversion from number of light quanta incident on the film to optical density. This will affect the magnitude of the NPS, but not its shape. Therefore, we compared the shapes of the NPS for our simulated image and for the Min-R 2000 system (see Figure 11). There is good agreement – less than 8% difference except at high spatial frequencies. Since we have not included film granularity in our simulated image, we would expect that our simulated image would have lower NPS at high spatial frequencies.

We have also made simulated images of the phantoms. The phantoms were first imaged on Kodak XV film (non-screen system) using three times geometric magnification that will produce a high fidelity image, with low noise. The images taken on the XV film are digitized at 50-micron pixel resolution. This produces an image with effective pixel size of 17 microns. The resulting image is put through our simulation model to produce an image with the same exposure as used for the standard mammography system – a Kodak Min-R 2000 system.

To compare the simulated image to the screen-film image, we digitized the screen-film image at 50 microns and construct a 50-micron resolution simulated image (see Figure 12). Visually the real and the simulated images look similar, except that the simulated image is slightly darker than the real image. This is caused by using an incorrect conversion from number of light quanta to film optical density. We are now in the process of correcting this problem after discussion with Dr. Phillip Bunch of Eastman Kodak Company.
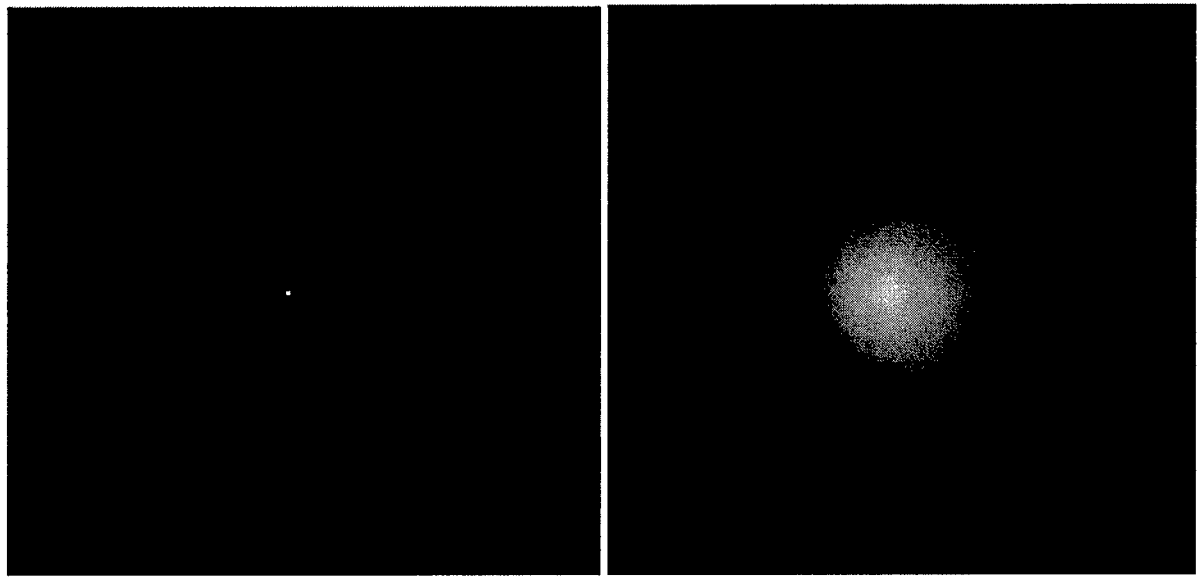
Figure 8. The input point image is shown on the left, the resulting output of our simulation model shown on the right. This point spread function is then subjected to a 2D fast Fourier transform to calculate the modulation transfer function (MTF) for the modeled phosphor screen (Min-R 2000).
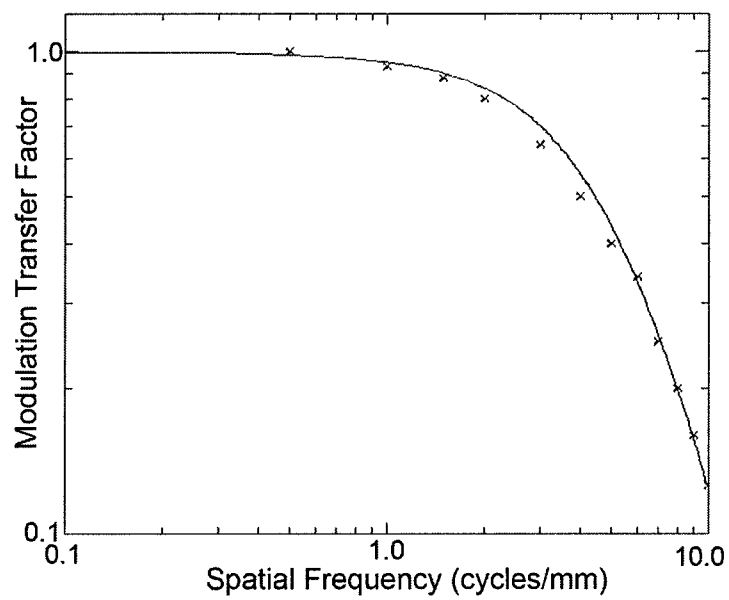

Figure 9. MTF curves for a Kodak Min-R 2000 screen-film system (x's), from published data [Bunch 1999] and from the simulated imaged (solid line) shown in Fig. 8.
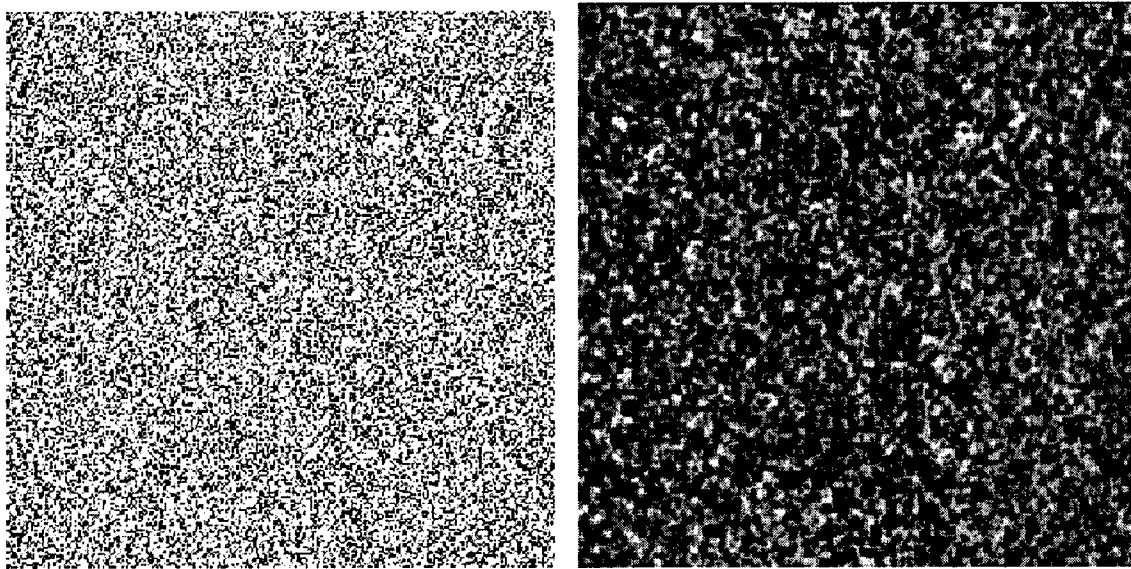
Figure 10. The image on the left contains uniform uncorrelated Gaussian noise and is used as input to our simulation model. The image on the right is the output of the model. This image and others like it are used to calculate the noise power spectrum.
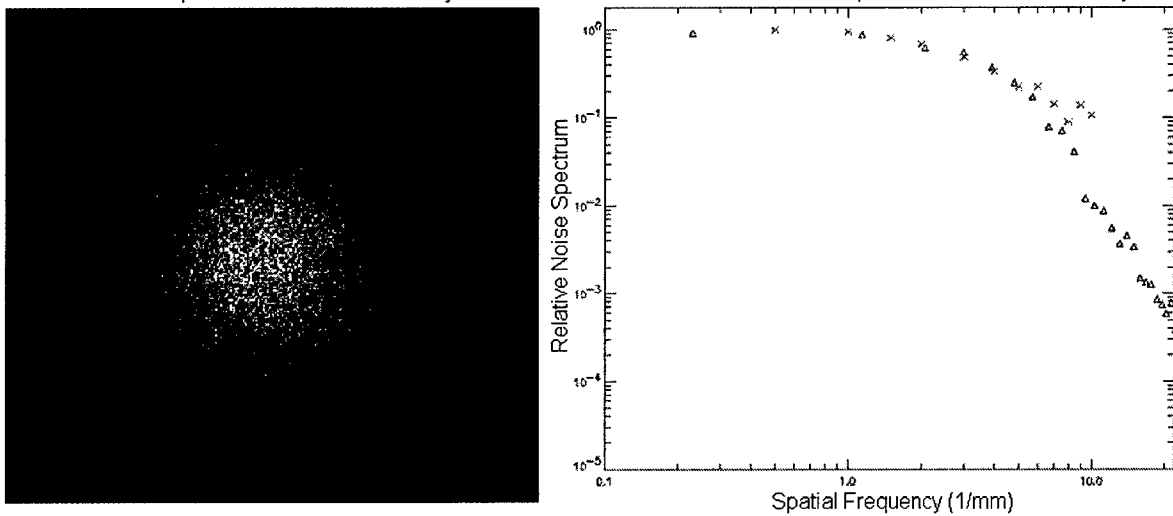

Figure 11. The image on the left is the 2D noise power spectrum of the output of the simulation model for a uniform noisy input (see Figure 10). The graph shows a slice through the 2D noise power spectrum (black triangles) and compares the simulated noise power spectrum to a Kodak Min-R 2000 system provided to us by P. Bunch (red x's). There is good agreement up to approximately 5 cycles/mm. The discrepancy at higher spatial frequencies is because the simulation result does not include the effects of film noise as the experimental result does.

15
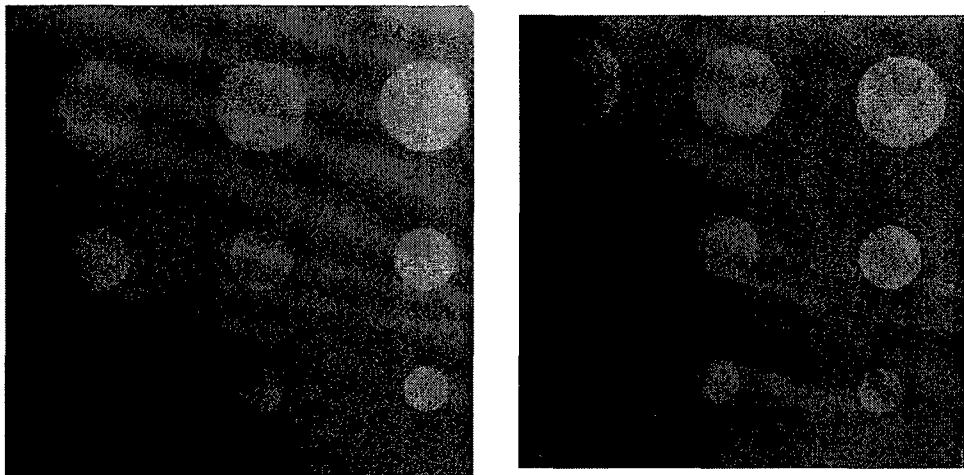
Figure 12. Comparison of real image (left side) and simulated phantom image (right side) of a portion of a contrast-detail phantom. The real image was made using a Kodak Min-R 2000 screen-film system and was digitized at 50-micron pixel resolution

5.1.4. Evaluation of simulated mammograms

This has not yet been accomplished, but we plan to test whether radiologists can tell the difference between our simulated and real mammograms. We will perform an observer study involving 8 radiologists in a two-alternative forced choice (2-AFC) experiment [Green 1974]. The radiologists will view a pair of mammograms, actually sections of a mammogram. One will be a simulated image and one will be a real image. The radiologist will have to choose which one is the real mammogram. To determine the number of cases needed, we will first perform a pilot study using 100 cases and 3 medical physicists who have worked in mammography for more than 7 years. We will use standard methodology for performing and analyzing the experiment [Green 1974; Loo 1984].

The images will be viewed on a pair of calibrated and identical CRT monitors. It would be ideal to compare the original screen-film mammogram to the simulated image printed on film. However, we believe that the printed image would look obvious compared to the real mammogram and thus bias the experiment.

5.2. Recommendations in relation to the Statement of Work

There were two changes to our statement of work. The first was to use cadaver breasts instead of mastectomy samples, since it is easier to get cadaver breasts. The second is we investigated the role of k-fluorescence reabsorption in our model. This physical phenomenon is

important in the newer phosphors used in digital mammography.

6. KEY RESEARCH ACCOMPLISHMENTS

- Method for simulating mammograms developed

- Linear systems model of a phosphor-based detector has been refined.

- New understanding of the effect of k-fluorescence reabsorption on the noise power spectrum of phosphor-based detectors

7. REPORTABLE OUTCOMES

We have presented parts of this work at one national and three international conferences. We have published one conference proceeding (attached) and we are working on three papers for peer-reviewed journals (2 are attached).

Oral Presentation

1. Nishikawa RM and Lee S: A Method for Producing Simulated Mammograms. Presented at the Presented at the 42nd Annual Meeting of the American Association of Physicists in Medicine, July 2002, Montreal PQ.

2. Nishikawa RM and Lee S: A method for producing simulated mammograms. Presented at the 7th International Conference on Digital Mammography, June 2002, Bremen, Germany

3. Zhang Y, Nishikawa RM: Computer Simulation of Mammographic Imaging for Applications in CAD. Presented at 5th International Workshop on Computer-Aided Diagnosis. June 2004, Chicago, IL.

4. Chinander MA, Nishikawa RM, Zhang Y: Numerical simulation of mammographic imaging system and assurance checking. Presented at 90th Scientific Assembly and Annual Meeting of the Radiological Society of North America, November 2004, Chicago, IL.

Conference Proceedings

1. Zhang Y, Nishikawa RM: Computer Simulation of Mammographic Imaging for Applications in CAD. Proc. CARS 2004 (in press).

Manuscripts in Preparation for peer-reviewed Journal
We are preparing 3 manuscripts to be submitted for peer-review. Two are in intermediate draft form and are attached. We are still working on the first draft of the third paper.

1. Zhang Y, Nishikawa RM: Numerical Simulation of Mammographic Imaging System. To be submitted to Medical Physics. (draft attached)
2. Zhang Y, Nishikawa RM: 3D Modeling and Simulation of Characteristic x-ray re-absorption by Monte Carlo Simulation. To be submitted to Computers in Medicine and Biology. (draft attached)
3. Nishikawa RM, Zhang Y, Chinander MA: Effect of the finite thickness of a phosphor screen and k-fluorescence reabsorption on image quality. To be submitted to Medical Physics. (in preparation)

8. CONCLUSIONS

We are now capable of producing simulated mammograms. The resolution and noise properties are closely matched to those of real images. We are still improving the model with the addition of film noise, scattered radiation, and light quanta to film optical density conversion. In addition, we have included the effects of k-fluorescence reabsorption in our model. This will allow us to better simulate a wider variety of detectors used in mammography.

We have also shown for the first time that the finite thickness of the screen will increase the effect of k-fluorescent re-absorption. When the phosphor is treated as a single thick slab, k-fluorescence re-absorption reduces the noise power spectrum by about 20%. When the phosphor is more accurately modeled as being a stack of many thin layers, k-fluorescence re-absorption reduces the noise power spectrum by about 70%.

As was in our original statement of work, we still plan to conduct an observer study to show that the simulate images look like real mammographic images. Currently, we have funding through a training grant for a post-doctoral fellow to continue the work for one year. We will conduct the observer study and make further refinements to the model.

9. REFERENCES

Boone JM, Seibert JA, Tang C-M, and Lane SM. 2002. Grid and Slot Scan Scatter Reduction in Mammography: Comparison by Using Monte Carlo Techniques. *Radiology* 222: 519–527.

Bunch PC. 1999. Advances in high-speed mammographic image quality. *Proc SPIE* 3659: 120-130.

Green DM, and Swets JA. 1974. *Signal Detection Theory and Psychophysics* (Wiley, New York).

Hillen W, Eckenbach W, Quadflieg P, and Zaengel TT. 1991. Signal-to-noise performance in cesium iodide x-ray fluorescent screens. *Proc SPIE Medical Imaging* 1443: 120-131.

Loo L-ND, Doi K, and Metz CE. 1984. A comparison of physical image quality indices and observer performance in the radiographic detection of nylon beads. *Phys Med Biol* 29: 837-856.

Metz CE, and Vyborny CJ. 1983. Wiener spectral effects of characteristic x-ray reabsorption in radiographic screen-film systems. *Physics and Medicine in Biology* 28: 547-564.

Nishikawa RM, and Yaffe MJ. 1989. Effect of finite phosphor thickness on detective quantum efficiency. *Med Phys* 16: 773-780.

Nishikawa RM, and Yaffe MJ. 1990a. Effect of various noise sources on the detective quantum efficiency of phosphor screens. *Med Phys* 17: 887-893.

Nishikawa RM, and Yaffe MJ. 1990b. Model of the spatial frequency-dependent detective quantum efficiency of phosphor screens. *Med Phys* 17: 894-904.

Van Metter R, Dillion P, Huff KE, and Rabbanni M. 1986. Computer simulation of radiographic screen-film images. *Proc SPIE* 626: 82-99.

Yao J, and Cunningham IA. 2001. Parallel cascades: New ways to describe noise transfer in medical imaging systems. *Med Phys* 28: 2020-2038.

Numerical Simulation of Mammographic Imaging System

Yinghui Zhang and Robert M. Nishikawa

Department of Radiology, the University of Chicago

Abstract: A method is described for the computer simulation of mammographic imaging. Software has been developed to simulate the physics processes of converting input x-ray quanta to visible light photons inside a fluorescent intensifying screen. The simulation algorithm is based on the model of the spatial-frequency-dependent detective quantum efficiency of fluorescent screens, which was developed previously. The x-ray input to the simulation software was derived from images taken on directly contacting film by calibrating the film optical density to the x-ray exposure incident to the film. The physics processes that convert x-ray quanta to visible light photons inside a fluorescent screen were simulated by five mathematical transformations. Standard FFT techniques were used. Swank's one-dimensional fluorescent screen modulation transfer function model was extended into a two-dimensional photon diffusion model by solving a 2-dimensional Boltzmann diffusion equation. During simulation computation, the intensifying fluorescent screen was conceptually divided into multiple thinner sub-layers. The final image was obtained by integrating the visible light output of every sub-layer over the whole intensifying screen. The software based on the simulation algorithm in this paper was tested for assurance by three comparisons: phantom images, modulation transfer function, and noise power spectrum. All test results showed that the simulation method and the simulation software worked correctly. Qualitatively, the simulated and actual images of test objects looked similar. For the modulation transfer function and the shape of the noise power spectra, the difference between the simulation and the measured

values of an actual fluorescent screen was within 8%. Using the developed simulation technology, we will be able to produce simulated mammograms or other x-ray images that can be used to evaluate CAD methods and techniques.

1. Introduction:

Many research groups have been investigating CAD methods to help radiologists improve their detection and diagnosis of breast cancer from mammograms and various methods and technologies have been proposed [1~5]. A limitation to these quantitative mammogram analysis techniques is a lack of the set of standardized mammograms to evaluate the methods developed from different research labs. M. L. Giger [4] reviewed the computer-aided diagnosis in breast imaging and emphasized the importance to examine the performance of the CAD system and evaluate their ultimate contribution to the breast cancer diagnosis before using them in clinical practice. Although developing a common database of mammograms is helpful in solving the problem, the data set will still be less than ideal because the lack of accurate truth information (exact size, shape, and location) for the lesions in the mammograms. So, computer simulation technology is considered. In this paper, we propose a technology to numerically simulate the physics process of a mammographic imaging system. This technology can be used to generate simulated mammograms with truth information of lesions to evaluate CAD methods developed in labs.

The physics process we simulated is the conversion process from x-ray image input to visible light image output in most mammographic imaging systems. In clinical practice,

most mammograms are taken from a system that employs a fluorescent intensifying screen, as shown by **Figure 1**. In these systems, the x-ray quanta transmitted through the object, for instance, breast, impinge upon the fluorescent intensifying screen. The x-ray quanta that interact in the screen will excite the electrons from the valence band to the conduction band inside the screen. In an efficient screen, many of those electrons will emit visible light when returning to valence band. The fluorescent intensifying screen works as a linear transducer that converts absorbed x-ray quanta into light photons. The intensifying screen shown by **Figure 1** reduces the patient radiation dose compared to using x-ray film alone. However, it also has negative affect. First, the signal to noise ratio (SNR) of final x-ray images may be reduced slightly because the x-ray quantum noise may be transferred more efficiently than signals [6-8]. Secondly, the screen can also bring some special noise such as the screen-structure noise, secondary-quantum noise, etc [9, 10]. Thirdly, the scatter of the light photons created in the screen reduces spatial resolution of the final images. All these influences from the fluorescent intensifying screen are critical to diagnose small lesions at an early stage. So, it is important to simulate the physics processes inside the fluorescent intensifying screen accurately if using computer simulated images as the data to evaluate CAD technologies.

In this paper, we describe a method to numerically simulate the physics processes inside the fluorescent intensifying screen used in mammography. The method can also be used to simulate other x-ray imaging system using the x rays less than 40 keV. We developed software using this technology to simulate the conversion of x-ray quantum to visible light photons inside the fluorescent intensifying screen. This work was based on the model of the spatial-frequency-dependent detective quantum efficiency of phosphor

screens that we had previously [9, 10]. The technology can be used to generate the simulated x-ray image with accurate truth information for lesions.

2. Simulation Model

The model of the spatial-frequency-dependent detective quantum efficiency of phosphor screens uses six stages to describe the physics processes inside a fluorescent intensifying screen [3]. The physics processes of converting x-ray quanta to light photons inside a fluorescent screen are separated into two elementary processes: amplification process and scattering process [11]. Stages 1 to 4 form a quantum number amplification process and stages 5 and 6 form a photon scattering process. Because we limited our simulation to mammographic imaging system or x-ray imaging systems using the x rays less than 40 keV, the K or L fluorescence of the screens can be ignored.

The first stage is where x-ray quanta are incident on a fluorescent intensifying screen of thickness T. We use u($\vec{r}_{i,j}$, E) to express the distribution of x-ray fluence in this stage, where $\vec{r}_{i,j}$ is a two-dimensional vector describing a pixel position when x-ray quanta with energy E are incident on the screen. If the pixel size is Δa in both width and height and using i as the horizontal index and j as the vertical index, we have

$\vec{r}_{i,j} = \Delta a \times i \vec{i} + \Delta a \times j \vec{j}$. $\vec{i}$ is the unit vector in horizontal direction and $\vec{j}$ is the unit vector in vertical direction. The second stage is the fraction of the input quanta that interact in the fluorescent screen. We use $v(\vec{r}_{i,j}, E)$ to express the distribution of the x-ray quanta that will interact in the screen after entering the screen at a pixel area Δa. The third stage is where x-ray quanta will interact at different depths, t, inside the fluorescent screen. We use $w(\vec{r}_{i,j}, t, E)$ to express the distribution of x-ray quanta in a voxel $\Delta a \Delta t$, centered at

$(\vec{r}_{i,j}, t)$, at this stage. The fourth stage is where the absorbed x-ray energy is partially

converted into light photons. We use $x(\vec{r}_{i,j}, t)$ to express the distribution of the light

photons created at this stage. From stage 1 to stage 4, the input x-ray quanta become

visible light photons. Because the energy of light photons is much smaller than that of x-

ray quanta, the number of visible light photons is much larger than the number of primary

input x-ray quanta. So, stage 1 to stage 4 forms a quantum number amplification process.

$u(\vec{r}_{i,j}, E)$ is the input of this quantum number amplification process and $x(\vec{r}_{i,j}, t)$ is the

output of this quantum number amplification process.

The fifth stage is the fraction of light photons created at each voxel that escape to the

output surface of the intensifying screen. The photon distribution after this escape can be

expressed as $y(\vec{r}_{i,j}, t)$. The sixth stage is where the photons escaping spread over the

output and give the final light output. The distribution of photons can be expressed

as $z(\vec{r}_{i,j}')$, where $\vec{r}_{i,j}'$ is the position vector of an output light image pixel. These two stages

form the scattering process of the light photons created inside the screen and characterize

scattering and absorption of the light photons created from the energy of input x-ray

quanta as shown by **Figure 2**. Swank [12] derived a formula to calculate an 1-

dimensional modulation transfer function [MTF(f)] for modeling the diffusion and

absorption process of light photons inside phosphor by assuming an 1-dimensional (line)

input source. To simulate the 2-dimensional mammograms or other x-ray images, a

formula to modeling 2-dimensional modulation transfer function of diffusion and

absorption of light photon is required. We derived this formula, Equation (1), using the

same method as Swank used (please see **Appendix A**). In fact, Equation (1) is the

solution of Boltzmann differential equation in spatial frequency domain.

$$\varphi_{u,v}(u,v,t) = \frac{\tau\rho_1[(\omega + \tau\rho_0)e^{\omega t} + (\omega - \tau\rho_0)e^{-\omega t}]}{(\omega + \tau\rho_0)(\omega + \tau\rho_1)e^{\omega T} - (\omega - \tau\rho_0)(\omega - \tau\rho_1)e^{-\omega T}} \quad (1)$$

where $\varphi_{u,v}(u,v,t)$ is the Fourier Transformation of the product of light photon density

and diffusion coefficient (**see Appendix A;**) u and v are spatial frequency; t is the depth

inside a fluorescent screen; τ is the inverse relaxation length that describes the probability

of optical absorption occurring; ω is related to spatial frequency and

$\omega^2 = \sigma^2 + 4\pi(u^2 + v^2)$ where σ is the reciprocal diffusion length and characterizes

optical scattering; T is the thickness of the screen; $\rho_i = \dfrac{1 - r_i}{1 + r_i}$ where r_i is the reflectivity of

the boundary of the screen; ($i = 0$) represents the interface closest to the x-ray source of

the screen and ($i = 1$) represents the output interface.

Equation (1) can be used to simulate scattering and absorption process of light

photons created inside a fluorescent intensifying screen. Parameters τ, ρ_0, and σ

depend on the type of the phosphor, the size and the shape of the phosphor crystals, the

absence or addition of some light absorbing materials, and the reflectivity of input and

output interfaces of the screen. Those parameters characterize the screens used in

mammographic imaging systems or other x-ray imaging systems.

Figure 3 shows two examples of $\varphi_{u,v}(u,v,t)$ function at different screen depths. The

parameters to calculate **Figure 3** are listed in **Table 1**. They are chosen to simulate a

Mini R 2000 intensifying screen. The left panel of **Figure 3** was calculated at screen

depth $t = 10\mu m$ and the right panel of **Figure 3** was calculated at screen depth $t = 80\mu m$.

Table 1 Simulation Parameters

X-ray Energy E	20.0 KeV
Pixel Size	$17 \times 17 \ \mu m^2$
Image Size	256×256 pixels
Linear Attenuation μ	37.7 1/mm
Conversion Coefficient ε	0.15
Screen Thickness T	85 μm
Reciprocal Diffusion Length σ	11 1/mm
Inverse Relaxation Length τ	50 1/mm
Input Ratio of Reflectivity ρ_0	0.90
Output Ratio of Reflectivity ρ_1	0.70
Sub-layer Thickness	1 μm

3. Simulation Algorithm

Our algorithm to simulate the physics processes inside a fluorescent intensifying

screen is to conceptually divide the fluorescent screen into multiple thin sub-layers shown

by **Figure 4**. Each sub-layer is thin enough to be of a fixed depth t. The closer to the

input surface of the screen the sub-layer is, the higher the input x-ray fluence to the sub-

layer is. The diffusion and absorption of light photons created at each sub-layer depend

on how far the sub-layer is from the output surface of the screen. There will be more light

photons diffused and absorbed if the sub-layer is far from the output surface of the screen.

We used five cascading mathematical transformations to simulate the physics processes

of converting x-ray quantum input to the final light image output at each sub-layer. The

output light fluence of the whole intensifying screen was considered as the accumulation

of the light output of every sub-layer. The simulation software integrates the light outputs

of all sub-layers into a final output image of the phosphor screen.

The five cascading transformations used are x-ray interaction mathematical transformation, x-ray quantum to light photon transformation, Fourier transformation, light photon escape and scattering transformation, and inverse Fourier transformation.

The first transformation used was x-ray interaction mathematical transformation. It simulates the physics process from stage 1 to stage 3 of the model of the spatial-frequency-dependent detective quantum efficiency of phosphor screens [9, 10]. If the number of x-ray quanta is N_0 before the x-ray beam is incident to the voxel centered at (x, y) of a sub-layer thick Δt at depth t, according to linear attenuation theory [13], the number of x-ray quanta penetrating the voxel is

$$N = N_0 e^{-\mu \Delta t} \qquad (2)$$

where N is the number of the x-ray quanta penetrating from this voxel; μ is the linear attenuation coefficient of the intensifying screen; Δt is the thickness of the sub-layer concerned. From Equation (2), we can get the number of the x-ray quanta removed from the beam in the voxel observed:

$$\Delta N = \mu N \Delta t = \mu N_0 \Delta t e^{-\mu \Delta t} \qquad (3)$$

where ΔN is the number of the x-ray quanta removed from the beam after it incidents to the voxel centered at (x, y) of the sub-layer at depth t of the screen.

From Equation (3), we can get the fraction, $P_{removingX-ray}$, that the x-ray quanta are removed from the beam at the voxel centered at (x, y) and at depth t of the intensifying screen. It can be expressed as

$$P_{removingX-ray} = \frac{\Delta N}{N_0} = \mu \Delta t e^{-\mu \Delta t} \qquad (4)$$

Using this $P_{removingX-ray}$, the x-ray interaction mathematical transformation can be expressed as Equation (5).

$$w(x, y, E, t) = \mu \Delta t e^{-\mu \Delta t} u(x, y, E) \qquad (5)$$

The second mathematical transformation was x-ray quantum to light photon transformation. It simulates the creation of the light photons from the absorbed energy of x-ray quanta. According to the assumptions of the model of spatial-frequency-dependent detective quantum efficiency of phosphor screens, every photon created inside the screen has energy 2.4 eV or 2.4×10^{-3} keV [10, 14]. Then, the number of photons created by absorbing one x-ray quantum with energy E is

$$q(x, y, t) = \frac{E}{2.4 \times 10^{-3}} \varepsilon w(x, y, E, t) \qquad (6)$$

where $q(x, y, t)$ is the distribution of photons created by absorbing x-ray quanta; E is the energy of the x-ray quantum in keV; ε is the conversion coefficient of the screen [10].

Mathematical transformations 3 to 5 simulate the diffusion and absorption of the photons created inside the intensifying screen. These photons need to escape from absorption, diffusion, and reflection before contributing to the output light image. We can use Equation (1) to simulate the affects of this escape. However, Equation (1) is the solution of the Boltzmann diffusion equation in spatial frequency space (please see **Appendix A**). We either use Equation (1) as a kernel to do convolution with the output of transformation 2 or transform the output of transformation 2 into spatial frequency space. To save the computation time from convolution, we transform the output of the second transformation into spatial frequency space. We used standard 2-demisonal FFT

technology to do this transformation [15]. So, our third mathematical transformation used was a Fourier transformation shown by Equation (7)

$$Q(u,v,t) = F\{q(x,y,t)\} \qquad (7)$$

where u is the spatial frequency in horizontal direction; v is the spatial frequency in vertical direction. t is the depth position of the sub-layer.

The fourth mathematical transformation used was in spatial frequency domain and written as:

$$Z(u,v,t) = Q(u,v,t)\varphi_{u,v}(u,v,t) \qquad (8)$$

where $Z(u, v, t)$ is the Fourier Transformation of the final output image; $\varphi_{u,v}(u,v,t)$ is defined in Equation (1).

The fifth mathematical transformation used was an Inverse Fourier Transformation shown by Equation (9).

$$z(x',y',t) = F^{-1}\{Z(u,v,t)\} \qquad (9)$$

where $z(x',y',t)$ is the final output image from the concerned sub-layer at depth t of the intensifying screen.; (x',y') is the pixel position on the output interface of the intensifying screen. **Figure 5** shows the five cascading mathematical transformations in our simulation software.

Figure 6 shows the data flow of our x-ray imaging simulation software. Users can set characteristics of the fluorescent intensifying screen, select x-ray inputs, and assign the thickness of the sub-layer through user interface. After loading the x-ray input data and initializing the simulation system according to user's selection, the simulation software transfers the pixel values of the input x-ray image into the number of x-ray quanta. Then, the simulation kernel comes into the computation loops of sub-layers. In

each loop, the simulation software first sets the thickness of the sub-layer and its depth position in the intensifying screen. Then, the simulation software performs the five mathematical transformations to the input x-ray image data. Finally, the simulation software accumulates the output of each sub-layer to the output buffer. After processing the current sub-layer, the simulation software checks if there are more sub-layers required to be dealt with. If there are untreated sub-layers, the simulation software comes into the next loop of sub-layer computation. Otherwise, the program goes into the output operation. The output operation includes transforming the number of light photons into optical densities, buffering the data, etc.

4. Simulation Input and Output

The x-ray input of the simulation software is obtained by calibrating the directly contacting film x-ray images. We first made a step image using directly contacting x-ray film to calibrate the x-ray exposure and pixel values. The exposure for every step was recorded when we made the step image. After developing the step image film, we measured the optical density of the step image film and digitized the step image film into a 12 bit 4000x5000 digital image. On this digital image, every step corresponds to a pixel value. By the exposure records, we built the relationship between pixel values and x-ray exposures as shown by **Table 2**. The smallest pixel value is 0 and the biggest pixel zero is 4095. According to the relationship between x-ray exposure and x-ray quantum number, we get the x-ray quantum number for every special pixel value of our digitalized step image [16]. From reference [17] and our own test, we used $4.4 \times 10^{11} \sim 6.9 \times 10^{11}$ $quanta /(mm^2 R)$ at 20 keV to transform the x-ray exposure into x-ray quantum number.

Table 2 X-ray exposure to pixel value

	Exposure (R)	Pixel Value	
Step 1	1.93	3570	
Step 2	1.07	3370	
Step 3	0.68	2984	
Step 4	0.47	2216	

During buffering the input x-ray image in simulation, the simulation software translates the pixel values of the selected x-ray digital image based on the calibration, using interpolating and extrapolating technology. When doing interpolation and extrapolation, we assume the x-ray exposure information is in the domain of the linear portion of the film's characteristic curve [17].

The simulation output image was obtained by transforming the number of light photons of each pixel into optical density using curve of optical density to photon fluence shown by **Figure 7**, taken from reference [17]. Then, the optical density was transformed into pixel value using the curve of the pixel value to optical density shown by **Figure 8**. This curve was obtained by calibrating a step x-ray image from an imaging system employing an intensifying screen.

5. Simulation Assurance

We used three methods to check our simulation algorithm and the simulation software. The three testing methods are: using known images, checking the modulation transfer function of the simulation software [18-21], and checking the noise power spectrum [22-26] of the simulation software. To compare with the measured modulation transfer function and noise power spectrum from Mini R 2000 screen-film system, we set the simulation parameters as listed in **Table 1**.

Figure 9 and **Figure 10** show the comparison of the simulated image with the x-ray image taken from a Mini R 2000 screen-film mammographic imaging system. The left

panel of **Figure 9** is a phantom image taken from the real screen-film system. The right

panel is a simulated image of the same phantom object. The two images look similar. The

left panel of **Figure 10** is the display values from a row of a screen-film phantom image.

The width of its pixel is 50 μm. The right panel of **Figure 10** is the display values from a

row of a simulated image of the same phantom object. Because the width of the simulated

image is 17 μm, the display values plotted are average per 3 pixels. The comparison

shows that the simulated image has same imaging futures as the image from the real

screen-film mammographic imaging system.

To measure the modulation transfer function (MTF) of our simulation operation, we

first generated a point image using the computer. This image has only one bright pixel at

its center with the maximum pixel value 4095 which is corresponding to x-ray exposure

4.18R according to **Table 2**. This exposure is equal to about 4600 x-ray quanta if the

pixel size is 17$\mu m \times$17μm and the x-ray fluence is 6.9×10^{11} $quanta /(mm^2 R)$ at 20 keV.

We ran the simulation software using this point image as the x-ray input. Then, we did a

Fourier Transformation to the simulation output of this point image. According to the

definition of modulation transfer function, this Fourier Transformation is the modulation

transfer function of our simulation software. **Figure 11** shows the input point image and

the Fourier Transformation of the simulation output. The left panel of **Figure 11** is the

point image and the right panel is the Fourier transformation of the simulation output of

the point image. **Figure 12** shows the modulation transfer factor of our simulation

software, initialized with the parameters listed in **Table 1**, and the modulation transfer

factor measured from a Mini R 2000 intensifying screen. By comparing the modulation

transfer function of simulation software with the measured data, we can see that the

simulation software works correctly. The difference between the modulation transfer factor of our simulation software and the measured values is within 4%.

To obtain the quantum noise power spectrum of the simulation software, we created a noise image with the normal random number generator of MATLAB as the input of our simulation operation. We subtracted the mean from the simulation output and squared the result. Then, we did Fourier Transformation and divided the result by the maximum value in spatial frequency domain. **Figure 13** shows one of our noise input images and the simulation outputs. The left panel of **Figure 13** is the input noise image and the right panel is the output of the simulation. We can see the blurring resulting from the simulated conversion process from x-ray quanta to light photons and the scattering of light photons inside the simulated intensifying screen.

Figure 14 shows the relative noise power spectrum of our simulation software. The left panel is an original noise power spectrum of our simulation software from the measurement. The right panel of **Figure 14** shows the smoothed relative noise power spectrum of the simulation software and the measured relative noise power spectrum of a real screen. The measured data are from Kodak Min-R 2000 screen [23]. The smoothed relative noise power spectrum of simulation software is calculated by two steps of averaging computation. The first step is that we put 4 consecutive data of a relative noise spectrum into one group and calculated the average of every group. The second step is that we used 11 random noise input images as shown by the left panel of **Figure 13** and obtained 11 relative noise power spectra of simulation software. Then, we averaged the 11 spectra. We can see that the difference between the relative noise power spectrum of our simulation software and the measured values is within 8%.

6. Summary

This paper presented a method to simulate the physics processes of converting x-ray quantum image to visible light photon image inside a fluorescent intensifying screen based on previous work in modeling the quantum efficiency of the fluorescent intensifying screen. We divided the fluorescent intensifying screen into multiple thinner sub-layers and used five mathematical transformations to simulate the physics process of every sub-layer that converts the x-ray input quanta to light photons and the process of the diffusion, absorption, and reflectivity of the light photons. We integrated the light photons of every sub-layer over the whole screen into the final output image. Using the algorithm of this paper, we developed the simulation software in Linux operating system, using C++. Three methods were used to check our simulation technology. Qualitatively, the simulated and actual images of test objects looked similar. Quantitatively, the difference between our simulation software and the measured values of a real intensifying screen was within 4% in modulation transfer function and within 8% in relative noise power spectrum.

Based on this x-ray imaging system simulation technology, it is possible to generate some simulated mammograms or other x-ray images with accurate truth information for lesions. The simulated x-ray images can be used to evaluate computer aided diagnose (CAD) technology. The further work includes modeling the intensifying screen more accurately, measuring the linear attenuation coefficient of the malignant lesions and benign lesions accurately, and researching the algorithms to add the lesions to x-ray images for x-ray imaging simulation software. We also need to develop some algorithm

to simulate the more serious random noise of x-ray quanta in screen-film system than that of directly contacting film images.

7. Acknowledgement

Appendix A: Derivation of light photon diffusion and absorption model

The Boltzmann differential equation of photons created inside a screen can be written as Equation (A1) if the observed points are relatively far from the source (*i.e.* the distance between the observed point and source is larger than a mean free path) and the observed point is not close to the boundary [27].

$$\nabla^2 N_0(\vec{r}) - \frac{1}{L^2} N_0 + \frac{1}{D} S_0 = 0 \qquad (A1)$$

where N_0 is the particle density; S_0 is an isotropic source of particles; $\vec{r}$ is the position vector of the observed point; L is the diffusion length; D is the diffusion coefficient. Both L and D are related to the transport mean free path of the particles.

Inside a fluorescent screen (see **Figure 2**), the Boltzmann equation can be simplified into Equation (A2) by combining L and D into one coefficient: reciprocal diffusion length.

$$-\nabla^2 \phi(\vec{r}) + \sigma^2 \phi(\vec{r}) = S(\vec{r}) \qquad (A2)$$

where $\phi(\vec{r})$ is the product that the light photon density times the diffusion coefficient;

$S(\vec{r})$ is the source function; σ is the reciprocal diffusion length and $\sigma = \dfrac{D}{L^2}$.

If the input image is $u(x, y)$, the sampling of the input image can be expressed as

$$u^+(x, y) = u(x, y) \sum_{i,j} \delta(x - ia, y - ja) = \sum_{i,j} u_{i,j}(ia, ja)\delta(x - ia, y - ia) \quad (A3)$$

where $u^+(x, y)$ is a sequence of scaled δ functions. So, we only need to derive a

solution of Equation (A2) when the source is a 2-dimensional δ function.

If the source in Equation (A2) is a point source and $S(\vec{r}) = \delta(x)\delta(y)\delta(t - t_0)$, Equation

(A2) becomes

$$-\nabla^2\phi + \sigma^2\phi = \delta(x, y, t - t_0) = \delta(x)\delta(y)\delta(t - t_0) =$$
$$= \left(\frac{1}{2\pi}\int e^{iux}du\right)\left(\frac{1}{2\pi}\int e^{ivy}dv\right)\delta(t - t_0) \tag{A4}$$

In Equation (A4), we use a definition of δ function, Equation (A5), to substitute $\delta(x)$

and $\delta(y)$ [28].

$$\delta(x) = \frac{1}{2\pi}\int e^{i2\pi ux}du \tag{A5}$$

If we assume

$$\phi(x, y, t) = \frac{1}{4\pi^2}\iint \varphi_{u,v}(t)e^{i2\pi(ux+vy)}dudv, \tag{A6}$$

and substitute $\phi(x, y, t)$ of Equation (A4) with Equation (A6), we can get a new equation,

Equation (A7).(Please see **Appendix B**)

$$-\nabla_t^2\varphi_{u,v}(t) + [4\pi^2(u^2 + v^2) + \sigma^2]\varphi_{u,v}(t) = \delta(t - t_0) \tag{A7}$$

Equation (A7) is Equation (A4) in spatial frequency space. Using the same method as

Swank used [12], we can obtain Equation (1) as the solution of Equation (A7).

Appendix B: Derivation of Equation (A7)

Using Equation (A6), we can get Equation (B1) for operator ∇^2.

$$\nabla^2 \phi(x,y,t) = \nabla^2 \left(\frac{1}{4\pi^2} \iint \varphi_{u,v}(t) e^{i2\pi(ux+vy)} du dv \right)$$

$$= \frac{1}{4\pi^2} \iint \nabla^2 \left(\varphi_{u,v}(t) e^{i2\pi(ux+vy)} \right) du dv \qquad \text{(B1)}$$

In Equation (B1), we exchanged the order of derivative and integration.

Using Equation (B1) and Equation (A5), Equation (A4) can be rewritten into

$$-\frac{1}{4\pi^2} \iint \nabla^2 \left(\varphi_{u,v}(t) e^{i2\pi(ux+vy)} \right) du dv + \sigma^2 \frac{1}{4\pi^2} \iint \varphi_{u,v}(t) e^{i2\pi(ux+vy)} du dv$$

$$= \left\{ \frac{1}{4\pi^2} \iint e^{i2\pi(ux+vy)} du dv \right\} \delta(t - t_0) \qquad \text{(B2)}$$

Considering $\nabla = \frac{\partial}{\partial x}\vec{i} + \frac{\partial}{\partial y}\vec{j} + \frac{\partial}{\partial t}\vec{k}$, the derivative in Equation (B1) can be calculated

by Equation (B3)

$$\nabla \left(\varphi_{u,v}(t) e^{i2\pi(ux+vy)} \right)$$

$$= \varphi_{u,v}(t)(i2\pi u) e^{i2\pi(ux+vy)}\vec{i} + \varphi_{u,v}(t)(i2\pi v) e^{i2\pi(ux+vy)}\vec{j} + \frac{\partial \varphi_{u,v}(t)}{\partial t} e^{i2\pi(ux+vy)}\vec{k} \qquad \text{(B3)}$$

Using Equation (B3), we can get

$$\nabla^2 \left(\varphi_{u,v}(t) e^{i2\pi(ux+vy)} \right)$$

$$= \nabla \left\{ \varphi_{u,v}(t)(i2\pi u) e^{i2\pi(ux+vy)}\vec{i} + \varphi_{u,v}(t)(i2\pi v) e^{i2\pi(ux+vy)}\vec{j} + \frac{\partial \varphi_{u,v}(t)}{\partial t} e^{i2\pi(ux+vy)}\vec{k} \right\}$$

$$= \varphi_{u,v}(t) \left[-4\pi^2 u^2 \right] e^{i2\pi(ux+vy)} + \varphi_{u,v}(t) \left[-4\pi^2 v^2 \right] e^{i2\pi(ux+vy)} + \frac{\partial^2 \varphi_{u,v}(t)}{\partial t^2} e^{i2\pi(ux+vy)} \qquad \text{(B4)}$$

$$= -4\pi^2 \left(u^2 + v^2 \right) \varphi_{u,v}(t) e^{i2\pi(ux+vy)} + \left(\nabla_t^2 \varphi_{u,v}(t) \right) e^{i2\pi(ux+vy)}$$

In Equation (B4), we defined $\nabla_t^2 = \frac{\partial^2}{\partial t^2}$.

Using Equation (B1) and Equation (B4), we can rewrite Equation (A4) into:

$$-\frac{1}{4\pi^2}\iint\left\{-4\pi^2\left(u^2+v^2\right)\varphi_{u,v}(t)e^{i2\pi(ux+vy)}+\left(\nabla_t^2\varphi_{u,v}(t)\right)e^{i2\pi(ux+vy)}\right\}dudv$$

$$+\sigma^2\frac{1}{4\pi^2}\iint\varphi_{u,v}(t)e^{i2\pi(ux+vy)}dudv=\left\{\frac{1}{4\pi^2}\iint e^{i2\pi(ux+vy)}dudv\right\}\delta(t-t_0)$$

$$(B5)$$

Combining the integration on the left of Equation (B5) and writing $\delta(t-t_0)$ into the integration on the right of Equation (B5), Equation (B5) becomes:

$$\frac{1}{4\pi^2}\iint\left\{-\nabla_t^2\varphi_{u,v}(t)+[4\pi^2(u^2+v^2)+\sigma^2]\varphi_{u,v}(t)\right\}e^{i2\pi(ux+vy)}dudv$$

$$=\frac{1}{4\pi^2}\iint\delta(t-t_0)e^{i2\pi(ux+vy)}dudv$$

$$(B6)$$

From Equation (B6), we can get Equation (A7) or (B7) with $\omega^2=4\pi^2(u^2+v^2)+\sigma^2$

$$-\nabla_t^2\varphi_{u,v}(t)+\omega^2\varphi_{u,v}(t)=\delta(t-t_0) \qquad (B7)$$

Reference:

[1] R. M. Nishikawa, "Detection of Microcalcification," Image Processing Techniques for Tumor Detection, edited by R. N. Strickland, Marcel Dekker Inc., New York, 131-154 (2002)

[2] M. L. Giger, Z. Huo, M. A. Kupinki, et al. Handbook of Medical Imaging, edited by M. Sonka and J. M. Fitzpatrick, "the Society of Photo-optical Instrumentation Enigneers, Bellingham, WA, Vol.2, 915 (2000)

[3] Y. H. Zhang and R. M. Nishikawa, "Computer Simulation of Mammographic Imaging for Application in CAD," CARS 2004 Computer Assisted Radiology and Surgery, Edited by H.U. Lemke, M.W. Vannier, K.Inarmura, A. G. Farman, K. Doi, and J.H. C. Reiber, ELSEVIER, 890-895 (2004)

[4]M. L. Giger, "Overview of Computer-Aided Diagnosis in Breast Imaging," Computer-Aided Diagnosis in Medical Imaging, edited by K. Doi, H. MacMahon, M. L. Giger, and K.R. Hoffmann. ELSEVIER SCIENCE B.V., 167-176 (1999)

[5]N. Ibrahim, H. Fujta, T. Hara, and T. Endo, "Automated detection of clustered microcalcifications on mammograms: CAD system application to MIAS database", Phys. Med. Biol. 42, 2577-2589 (1997)

[6]R. M. Nishikawa and M. J. Yaffe, "Digital Mammography", Med. Phys.

{6. M. J. Yaffe, "Digital Mammography", "Handbook of Medical Imaging Volume 1. Physics and Psychophysics", edited by J. Beutel, H. L. Kundel, and R. L. V. Metter, SPIE Press, Bellingham, Washington, 332-336 (2000) }

[7]M. Rabbani and R.V. Metter, "Some new applications of multivariate moment-generating functions to screen-film systems," Proc. SPIE 1090. 86-94 (1989)

[8]R. M. Nishikawa and M. J. Yaffe, "Effect of various noise sources on the detective quantum efficiency of phosphor screens," Medical Physics, Vol. 17, No. 5, 887-893 (1990)

[9]P. Bunch Med. Phys.

[10]R. M. Nishikawa and M. J. Yaffe, "Model of the spatial-frequency-dependent detective quantum efficiency of phosphor screens," Medical Physics, Vol. 17, No. 5, 894-904 (1990)

[11]M. Robbani, R. Shaw, and R. V. Metter, "Detective quantum efficiency of imaging systems with amplifying and scattering mechanisms", J. Opt. Soc. Am. A, Vol. 4, No. 5, 895-901 (1987)

[12]R. K. Swank, "Calculation of Modulation Transfer Functions of X-Ray Fluorescent Screens", Applied Optics, Vol. 12, No. 8, 1865-1870 (1973)

[13]H. E. Johns and J. R. Cunningham, "The Physics of Radiology", Charles C. Thomas Publisher, Springfield, Illinois, 134-137 (1983)

[14]P. C. Bunch, K. E. Huff, and R. V. Metter, "Analysis of the detective quantum efficiency of a radiographic screen-film combination", J. Opt. Soc. Am. A. Vol. 4, No. 5, 902-909 (1987)

[15]S. W. Smith, "The Scientist and Engineer's Guide to Digital Signal Processing", California Technical Publishing, San Diego, California, 225-236, (1999)

[16]V. N. Cooper, T. Oshiro, C. H. Cagnon, L. W. Baseett, T. M. Mcleod-stockmann, and N. V. Bezrukiy, "Evaluation of detector dynamic range in the x-ray exposure domain in mammography: A comparison between film-screen and flat panel detector systems," Med. Phys. 30 (10) 2614-2621 (2003)

[17]R. V. Metter, P. L. P. Dillon, K. E. Huff, and M. Rabbani, "Computer simulation of radiographic screen-film images", SPIE Vol. 626 Medicine XIV, PACS IV, 82-99 (1986)

[18]J. A. Cunningham, "Applied Linear-System Theory", "Handbook of Medical Imaging Volume 1. Physics and Psychophysics", edited by J. Beutel, H. L. Kundel, and R. L. V. Metter, SPIE Press, Bellingham, Washington, 97-130 (2000)

[19]C.E. Metz and K. Doi "Transfer Function Analysis of Radiographic Imaging Systems," Phys Med Biol 24, 1079-1106 (1979)

[20]K. Doi, K. Rossmann, and A.G. Haus, "Image Quality and Patient Exposure in Diagnostic Radiology," Photographic Science and Engineering 21, 269-277 (1977)

[21]J. T. Dobbins, "Effects of Undersampling on the Proper Interpretation of Modulation Transfer Function, Noise Power Spectra, and Noise Equivalent Quanta of Digital Imaging Systems," Medical Physics Vol. 22, No. 1, 171-181 (1995)

[22]I. A. Cunningham and R. Show, "Signal-to-noise optimization of medical imaging systems," J. Opt. Soc. Am A, Vol. 16, No. 3 621-632 (1999)

[23]R. M. Nishikawa and M. J. Yaffe, "SNR properties of mammographic film-screen system", Medical Physics, Vol. 12, No. 1, 32-39 (1985)

[24]M. L. Gier, K. Doi, and C. E. Metz, "Investigation of Basic Imaging Properties in Digital Radiography. 2: Noise Wiener Spectrum." Medical Physics Vol. 11, 797-905 (1984)

[24]J. H. Siewerdsen, I. A. Cunningham, and D. A. Jaffray, "A framework for noise-power spectrum analysis of multidimensional images," Med. Phys. Vol. 29, No.11, 2655-2671 (2003)

[26]W. Huda and R. M. Slone, "Review of Radiology Physics Second Edition" Lippincott Williams&Wilkins, Philadelphia, Pennsylvania, 71-72 (2003)

[27]R. E. Marshak, H. Brooks, and H. Hurwitz, Jr., "Introduction to Theory of Diffusion and Slowing Down of Newtrons-I", Nucleonics 4 (5), 10-22 (1949)

[28]G. B. Arfken and H. J. Weber, "Mathematical Methods for Physicists fourth edition", Academic Press San Diego, California, 81-87 (1995)
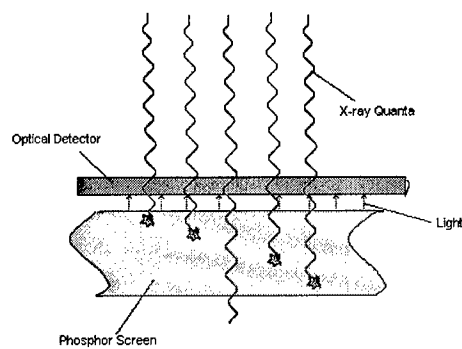
Figure 1: The x-ray imaging system employing a fluorescent intensifying screen.
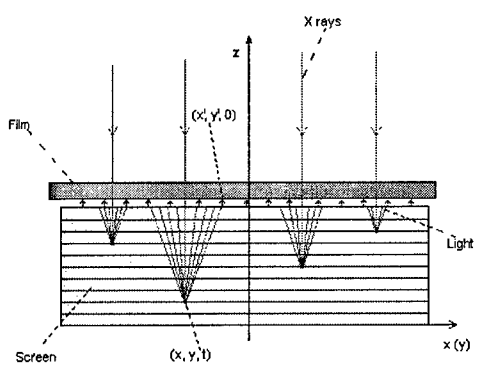
Figure 2 Diffusion of photons created by x-ray quanta. The photons created at

(x, y, t) may diffuse to $(x', y', 0)$.

φ(u,v) at 10 μm in a 85 μm screen   φ(u,v) at 80 μm in a 85 μm screen
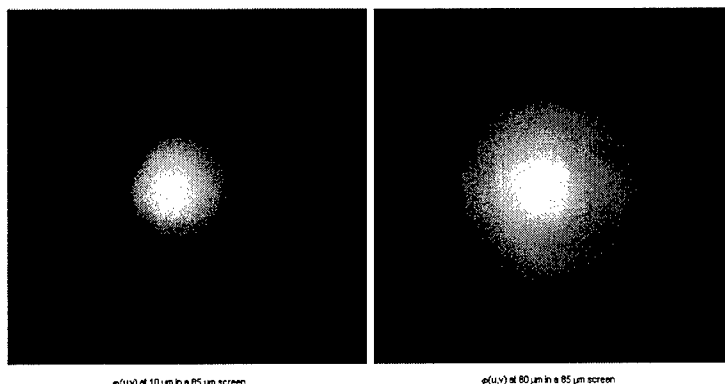
Figure 3 Photon diffusion and absorption function inside a fluorescent intensifying

screen with Equation (1). The parameters of the screen are listed in **Table 1**. The left

panel was calculated when $t = 10\,\mu m$ and the right panel was calculated when $t = 80\,\mu m$.
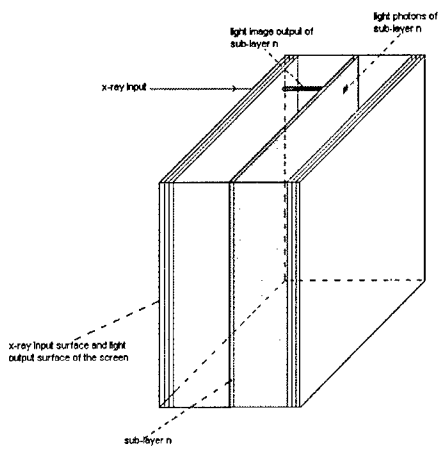
Figure 4 The fluorescent intensifying screen is conceptually divided into multiple thin sub-layers. All the sub-layers are independent of each other. Every sub-layer has different input x-ray fluence, absorbs different number of x-ray quanta, and outputs different light fluence. The diffusion and absorption of light photons of a sub-layer depend on how far the sub-layer from the output interface of the screen.
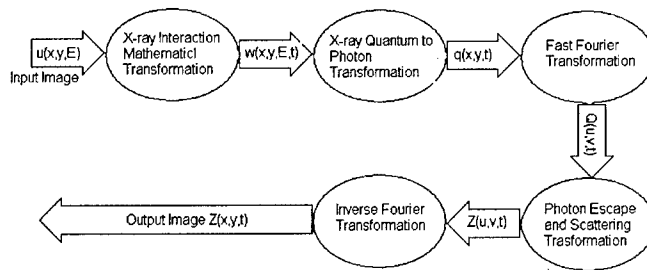
Figure 5 Five mathematical transformations used to simulate the processes of converting input x-ray quanta to light photons. The input x-ray image to every sub-layer will pass these five cascading mathematical transformations to contribute to the final output light image.
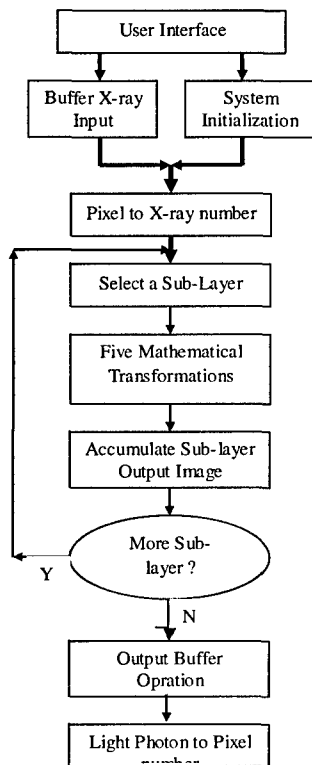
Figure 6 The data flow of the simulation. After buffering the x-ray input image and initializing the simulation system according to user's assignments, the simulation software goes into the loop to do the computation for every sub-layer of the intensifying screen. The final light image output of the whole intensifying screen is the accumulated output of all sub-layers.
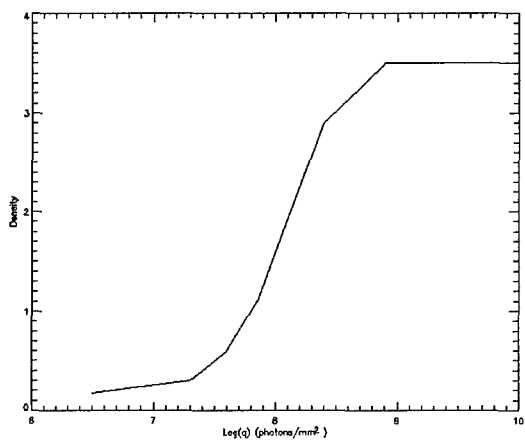
Figure 7 Density vs. log number of the light photons
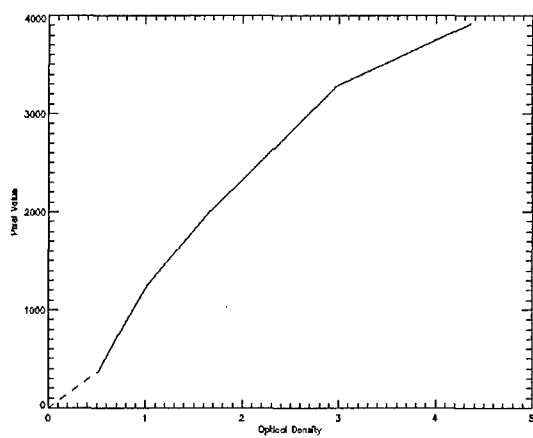
Figure 8 Pixel value vs. optical density
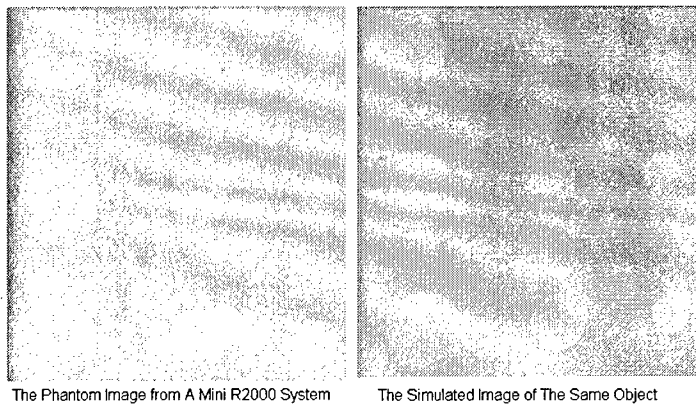
The Phantom Image from A Mini R2000 System   The Simulated Image of The Same Object

Figure 9 Comparison of the simulated phantom image with the image taken from a

screen-film system. The left panel is the image taken from a Mini R 2000 screen-film

system. The right panel is a simulated image.
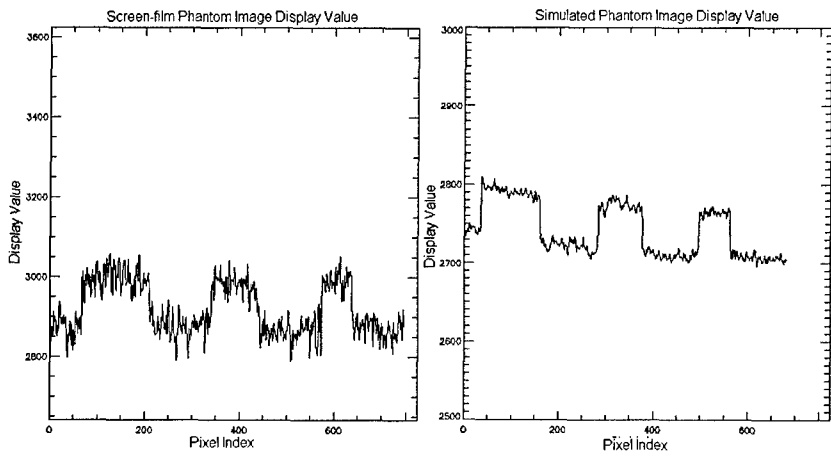
Figure 10 Comparison of the display values between the screen-film phantom image and simulated phantom image. The left panel is the display values from a row of screen-film phantom image. The right panel is the display value from a row of simulated image of the same phantom object.

Computer generated point image   The Fourier Transformation of the simulation output
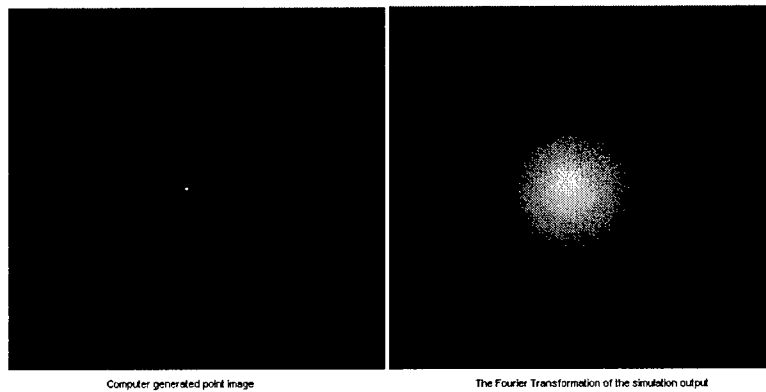
Figure 11 the measurement of the modulation transfer function of the simulation

software. The left panel is the input image used to measure the modulation transfer

function. The right panel is the Fourier transformation of the simulation output, the

modulation transfer function of the simulation software.
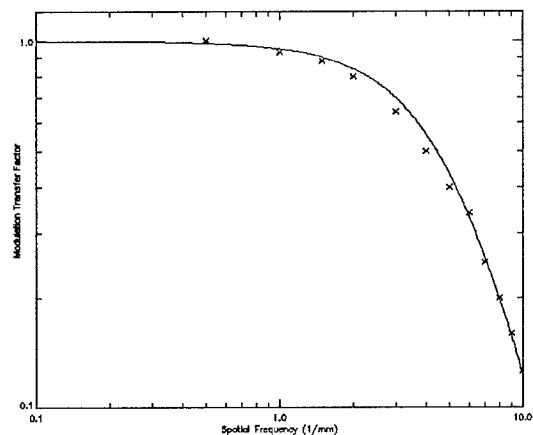
Figure 12 Comparison of the modulation transfer factor of the simulation software with

the measured modulation transfer factor. The solid curve is the modulation transfer factor

of the simulation software. [x] is the measured modulation transfer factor from a Min-R

2000 screen[23].

Input noise image   Output noise image
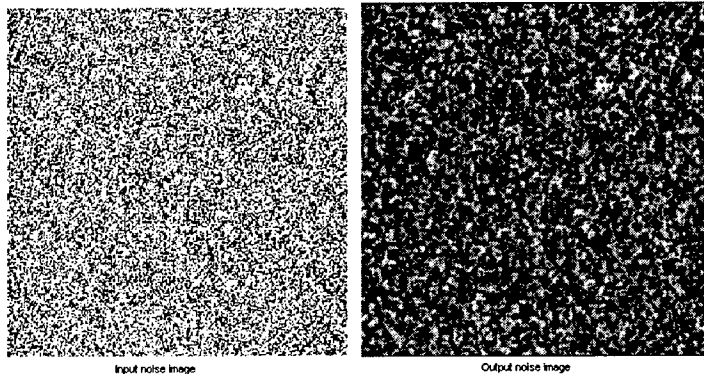
Figure 13 The noise images to measure the noise power spectrum. The left panel is the input noise image generated by a normal random number generator. The right panel is the output of the simulation software.
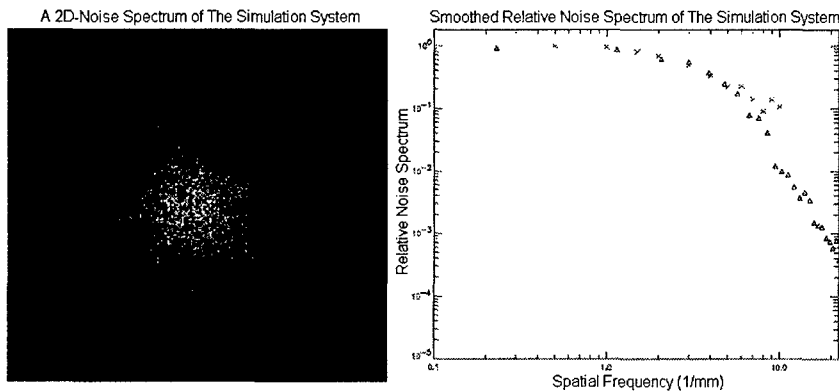
Figure 14 The noise power spectrum. The left panel is a 2D noise power spectrum of the

simulation software. The right panel compares the smoothed relative noise power

spectrum of the simulation software with the measured relative noise power spectrum

from a Mini R2000 intensifying screen. [Δ] is the relative noise power spectrum of the

simulation software. [x] is the relative noise spectrum measured from a Min-R 2000

screen [23].

3D Modeling and Simulation of Characteristic x-ray re-absorption by Monte Carlo Simulation

Yinghui Zhang PhD. and Robert M. Nishikawa PhD

The radiology department, the University of Chicago, IL 60637

Abstract

Many x-ray detectors use a phosphor screen to convert the x-ray quanta into visible light photons that are subsequently collected by an optical detector. Characteristic x rays can be produced within the phosphor. Some of these characteristic x-ray quanta are reabsorbed in the phosphor. This characteristic x-ray re-absorption affects the quality of images. In this paper, we developed a 3D convolution model to numerically simulate the characteristic x-ray re-absorption inside an image detector or intensifying screen with Monte Carlo technology. The 3D model is built through analyzing the physic process of creation, traveling, and absorption of characteristic x-ray quanta so that it can simulate the noise properties of characteristic x-ray re-absorption accurately. The phosphor layer of an image detector is conceptually divided into multiple sub-layers and every sub-layer is conceptually divided into multiple voxels based on the pixel size of a digital image. The 3D model computes the number distribution of reabsorbed characteristic x-ray quanta in every sub-layer using a pre-calculated convolution kernel. The convolution kernel gives the probability distribution that a characteristic x-ray quantum can be reabsorbed by a voxel. A cut-off window of convolution is calculated to reduce the computation time. This 3D convolution model shows that most characteristic x-ray re-absorption blurs the imaging. However, some of characteristic x-ray re-absorption enhances the primary x-ray input, depending on the relative position between the creation site and re-absorption site of the characteristic x rays. The simulation result is used to

quantitatively analyze the effect of the characteristic x-ray re-absorption on the imaging performance of the image detector or intensifying screen. The calculation to a Cesium Iodide layer with pixel size 17x17 μm^2 shows that the characteristic re-absorption may reduce the modulation transfer function of the image detector as much as 10% at some spatial frequency, which is close to the measurement. The model of the characteristic x-ray re-absorption in this paper can be combined to the model that simulates the whole imaging process of an image detector or intensifying screen to generate computer simulated x-ray images.

Keywords: image detector, intensifying screen, characteristic x rays, re-absorption, Monte Carlo simulation

1. Introduction

If the energy of incident x rays is above the K-edge of the phosphor layer inside an image detector or intensifying screen, characteristic x-ray radiation can be produced. Generally, these characteristic x rays are emitted isotropically and most likely reabsorbed at the projected position near the site where the incident x rays interact with the phosphor layer. However, some proportion of the characteristic radiation is reabsorbed at substantial distances from the initial interaction sites [1] and the re-absorption affects the quality of the images [2-4]. **Figure 1** schematically shows the re-absorption of characteristic x rays inside the phosphor layer of an image detector or intensifying screen, which blurs images. In **Figure 1**, characteristic x rays are generated from the interaction of incident x rays with the phosphor layer in the voxel centered at point A. These characteristic x rays isotropically emit inside the phosphor material. Some of these

characteristic x rays are reabsorbed in the phosphor voxel centered at point B, which results in visible light photons there. This means that Pixel **b** gets some visible light output because of the incident x rays at pixel **a**, which blurs the image.

The effect of characteristic fluorescence inside the phosphor layer of an image detector or intensifying screen on images has been researched 25 years ago. Vyborny et al emphasized that the escape of characteristic x rays from the intensifying screens should be taken into account when the efficiencies of screen-film systems were determined [5]. Arnold and Bjarngard experimentally observed the spread of line spread function (LSF) caused by K-characteristic x rays in rare earth phosphor intensifying screens [6]. Zhao et al found that the effect of K-fluorescent re-absorption on the imaging performance of *a-Se* digital mammography detectors can be significant [7]. Chan and Doi studied the x-ray energy absorption by Monte Carlo simulation [8]. There are also some investigators who used analytical methods to qualitatively calculate the energy deposited by the primary beam and by the reabsorbed K-characteristic x rays as an estimate of the total energy absorbed in the fluorescent intensifying screens [9-15]. All these investigations took the phosphor layer as a single thin layer and thus assumed the characteristic x rays transfer in a 2 dimensional plane. In this paper, we propose a 3D convolution model to calculate the number distribution of the reabsorbed characteristic x rays and a method to simulate the physical process of characteristic x-ray re-absorption with Monte Carlo technology in 3 dimensions. With this 3D convolution model and simulation method, we can accurately simulate the noise property of the characteristic re-absorption and quantitatively calculate the variation in modulation transfer function of an image detector or intensifying screen caused by the characteristic x-ray re-absorption. This 3D characteristic x-ray re-

absorption model can be combined to the model that simulates the whole imaging process of an image detector or intensifying screen to generate computer simulated x-ray images.

2. The model to calculate the number of the reabsorbed characteristic x rays

There are 3 assumptions in our model to calculate the number of the reabsorbed characteristic x rays inside the phosphor layer of an image detector or intensifying screen.

1) The phosphor layer of an image detector or intensifying screen is homogeneous.

2) The emission of the characteristic x rays created inside the phosphor layer is isotropic.

3) The predominant characteristic x rays are K-characteristic x rays. The characteristic x rays from other shells such as L shell are negligible comparing with the K-characteristic x rays.

As shown by **Figure 1**, the phosphor layer of an image detector or intensifying screen is conceptually divided into multiple thin sub-layers. All these sub-layers have the same thickness Δt. If the input x-ray fluence to the input interface of the phosphor layer is $S(x, y, 0)$, the x-ray fluence to a sub-layer at depth t will be $S(x, y, t)$ and

$$S(x, y, t) = S(x, y, 0)e^{-\mu t} \tag{1}$$

where μ is the linear attenuation coefficient of the incident x rays inside the phosphor layer.

If the pixel area of an image is $dxdy$, the number of x-ray quanta removed from the incident beam at a voxel $dxdydt$ centered at (x, y, t) is

$$dN(x, y, t) = \mu S(x, y, t)dxdydt = \mu S(x, y, 0)e^{-\mu t}dxdydt \tag{2}$$

With Equation (2), the number of K-characteristic x-ray quanta created in the voxel

centered at (x, y, t) can be expressed as

$$dn_k(x, y, t) = \xi\omega dN(x, y, t) = \xi\omega S(x, y)\mu e^{-\mu t} dxdydt \qquad (3)$$

where $dn_k(x, y, t)$ is the number of K-characteristic x-ray quanta created at phosphor

voxel centered at (x, y, t); ξ is the probability that an interacting x ray undergoes a K-

shell interaction; ω is the fluorescent yield of K-shell photoelectric interactions and

$S(x, y) = S(x, y, 0)$.

Since the K-characteristic x rays created inside the phosphor layer emit isotropically

from the sites where they are created, according to Equation (3), the fluence of the

characteristic x-ray quanta created in the voxel centered at (x, y, t) is, as shown by

Figure 2,

$$dI_k = \frac{dn_k(x, y, t)e^{-\mu_k \rho}}{4\pi\rho^2} \qquad (4)$$

The number of the characteristic x-ray quanta created in the voxel centered at (x, y, t) that

pass through spherical shell **1** in the phosphor layer, which is centered at (x, y, t) and with

radius ρ, will be

$$n_k \mid_\rho = \frac{dn_k(x, y, t)e^{-\mu_k \rho}}{4\pi\rho^2} 4\pi\rho^2 = dn_k(x, y, t)e^{-\mu_k \rho} \qquad (5)$$

In the same way, we can get the number of the characteristic x-ray quanta created at (x, y,

t) that pass through spherical shell **2**, which is with radius $\rho + d\rho$.

$$n_k \mid_{\rho+d\rho} = dn_k(x, y, t)e^{-\mu_k(\rho+d\rho)} \qquad (6)$$

From Equation (5) and (6), we can get the number of the characteristic x-ray quanta

created in the voxel centered at (x, y, t) that are removed from the fluence in the volume

between spherical shell **1** and spherical shell **2**. This number is

$$\Delta n_k = n_k \mid_\rho -n_k \mid_{\rho+d\rho} = dn_k(x,y,t)\{e^{-\mu_k\rho} - e^{-\mu_k(\rho+d\rho)}\} \qquad (7)$$

In Equation (7), if $d\rho \to 0$, the density of the characteristic x-ray quanta created in the

voxel centered at (x, y, t) in the volume between spherical shell**1** and spherical shell **2** is

$$\frac{\Delta n_k}{\Delta V} = \frac{dn_k(x,y,t)(e^{-\mu_k\rho} - e^{-\mu_k(\rho+d\rho)})}{4\pi\rho^2 d\rho} = -\frac{dn_k(x,y,t)}{4\pi\rho^2}\frac{d}{d\rho}(e^{-\mu_k\rho}) \qquad (8)$$

According to Equation (8), we can get the probability that the voxel centered at (x,y,t)

can reabsorb a characteristic x-ray quantum created in the voxel centered at (x, y, t), as

shown by **Figure 3**,

$$p(x',y',t',x,y,t) = \frac{1}{dn_k(x,y,t)}\frac{dn_k(x,y,t)}{4\pi\rho^2}\left|\frac{d}{d\rho}(e^{-\mu_k\rho})\right|dv' = \frac{1}{4\pi\rho^2}\mu_k e^{-\mu_k\rho}dv' \qquad (9)$$

where dv' is the volume of the voxel centered at (x',y',t'); ρ is the distance between the

creation phosphor voxel of the characteristic x-ray quanta and the observed phosphor

voxel that reabsorbs some of these characteristic x-ray quanta and

$$\rho = \sqrt{(x'-x)^2 + (y'-y)^2 + (t'-t)^2} \qquad (10)$$

If $\rho \to 0$, it means that the characteristic rays travel an infinitesimal distance and

attenuation is zero, thus $p(x',y',t',x,y,t) \to 0$ because there is no characteristic quantum

removed from the characteristic fluence in zero distance. If we use $dm_k(x',y',t',x,y,t)$ to

denote the number of the characteristic x-ray quanta created in the voxel centered at (x, y,

t) and reabsorbed by the voxel centered at (x',y',t'), using Equation (9), this number can

be expressed as:

$$dm_k(x', y', t', x, y, t) = p(x', y', t', x, y, t)dn_k(x, y, t) \qquad (11)$$

In fact, every voxel in the phosphor layer of an image detector or intensifying screen may

produce some characteristic x-ray quanta. Using Equation (3) and Equation (11), the total

number of reabsorbed characteristic x-rays by the voxel centered at (x', y', t') can be

expressed as

$$m_k(x', y', t') = \xi\omega\mu \iiint_{wholescreen} p(x', y', t', x, y, t)S(x, y, 0)e^{-\mu t}dxdydt \qquad (12)$$

where $m_k(x', y', t')$ is the total number of reabsorbed characteristic x-rays by the voxel

centered at (x', y', t'). The integration in Equation (12) is over the whole phosphor layer.

To calculate the integration of Equation (12) numerically, we can conceptually

divide the phosphor layer into multiple sub-layers that have the same thickness Δt. This

way, the whole phosphor layer becomes conceptually a set of voxels that have equal

volume $\Delta x \Delta y \Delta t$, where $\Delta x \Delta y$ is the area of an image pixel. Then, the integration of

Equation (12) can be written as

$$m_k(i', j', k') = \xi\omega\sum_{i}^{N_x}\sum_{j}^{N_y}\sum_{k}^{N_t} S(i, j)p(i', j', k', i, j, k)\mu e^{-\mu k\Delta t}\Delta x \Delta y \Delta t \qquad (13)$$

where (i, j, k) is the index of a source vexel where the characteristic x-ray quanta are

created; (i', j', k') is the index of the observed voxel that reabsorbs the characteristic x-ray

quanta from all other voxels; $S(i, j)$ is the input x-ray quantum distribution to the input

interface of the phosphor layer of an image detector or intensifying screens and

$S(i, j) = S(x, y)\delta(i\Delta x, j\Delta y)$, where $\delta(i\Delta x, j\Delta y)$ is a 2D delta function and $S(x, y)$ is the

primary x-ray input to image pixel (i, j); $p(i', j', k', i, j, k)$ is the probability that a

characteristic x-ray quanta created in voxel (i, j, k) is reabsorbed by voxel (i', j', k'); N_x,

N_y, and N_t are total voxel numbers in x, y, and t direction.

3. The reabsorbed characteristic x-rays that blur the image and enhance the primary x-ray input

In order to analyze the effect of the reabsorbed characteristic x-ray quanta on the imaging system, we can separate the integration domain of equation (13) into 2 parts, as shown by **Figure 4**. To any observed voxel (i', j', k'), domain A includes the voxels with $i \neq i'$ or $j \neq j'$ and domain B includes the voxels with $i = i'$ and $j = j'$. In fact, domain B is a phosphor bar from pixel $(i', j', 0)$ on the input interface to (i', j', T) on the bottom of the phosphor layer, and domain A includes all other voxels of the phosphor layer except the voxels of that phosphor bar.

The characteristic x-ray quanta created in the voxels of domain A are not related to the primary x-ray input to pixel $(i', j', 0)$ and do not contain image information to observed voxel (i', j', k') so that these characteristic x-ray quanta blur pixel $(i', j', 0)$. Then, we can call the re-absorption of these characteristic x-ray quanta as blurring characteristic x-ray re-absorption or crossing characteristic x-ray re-absorption because these characteristic x-ray quanta must have crossed at least one pixel boundary before arriving at voxel (i', j', k'). Re-absorption of characteristic x-ray quanta created in domain A is equivalent to voxel (i', j', k') s' obtaining some x-ray quanta from many blurring background x-ray sources.

The characteristic x-ray quanta created in the voxels of domain B are due to the primary x-ray input to pixel $(i', j', 0)$. These characteristic x-ray quanta do not cross any pixel boundary when arriving at the observed voxel (i', j', k'), as shown by **Figure 5**. The primary x-ray input at pixel $(i', j', 0)$ contains both image information and noise. But, the x-ray quanta containing image information and the x-ray quanta containing noise have the same energy distribution and have the same probability to create characteristic x rays. If there are more primary input x-ray quanta containing the image information, the re-absorption of the characteristic x-ray quanta created in domain B enhances the image information. If there are more noise quanta in the primary x-ray input to pixel $(i', j', 0)$, the re-absorption of the characteristic x-ray quanta created in domain B enhances noise. However, no matter if the characteristic x-ray quanta are created from noise x-ray input, re-absorption of characteristic x-ray quanta created in domain B is equivalent to voxel (i', j', k')'s getting more x-ray quanta from primary x-ray input at pixel $(i', j', 0)$ so that we can call this characteristic x-ray re-absorption as enhancing characteristic x-ray re-absorption.

Based on the analysis above, we can see that there are three types of x-ray input quanta to every voxel of phosphor layer when including characteristic x-ray re-absorption: the absorbed primary input x-ray quanta, the reabsorbed characteristic x-ray quanta enhancing the primary x-ray input, and the reabsorbed characteristic x-ray quanta adding the blurring background.

4. Convolution model of characteristic x-ray re-absorption

From Equation (9), we can have

$$p(i', j', k', i, j, k) = \frac{1}{4\pi\rho_{i',j',k',i,j,k}^2} \mu_k e^{-\mu_k \rho_{i',j',k',i,j,k}} \Delta x' \Delta y' \Delta t' \quad \text{when } \rho_{i',j',k',i,j,k} \neq 0$$

(14)

$$p(i', j', k', i, j, k) = 0 \quad \text{when } \rho_{i',j',k',i,j,k} = 0$$

$$\Delta x' = \Delta x, \Delta y' = \Delta y, \ \Delta t' = \Delta t \qquad (15)$$

$$\rho_{i',j',k',i,j,k} = \sqrt{(\Delta x)^2 (i'-i)^2 + (\Delta y)^2 (j'-j)^2 + (\Delta t)^2 (k'-k)^2} \qquad (16)$$

Using Equation (14) to (16), Equation (13) can be written into

$$m_k(i', j', k') =$$
$$\frac{\xi\omega(\Delta x \Delta y \Delta t)^2 \mu\mu_k}{4\pi} \sum_i^{N_x} \sum_j^{N_y} \sum_k^{N_t} S(i, j) \frac{e^{-(\mu k \Delta t + \mu_k \rho_{i',j',k',i,j,k})}}{\rho_{i',j',k',i,j,k}^2} \qquad \rho_{i',j',k',i,j,k} \neq 0 \qquad (17)$$

$$m_k(i', j', k') = 0 \qquad \qquad \rho_{i',j',k',i,j,k} = 0 \qquad (18)$$

Since $S(i, j)$ is not a function of index k, we can rewrite Equation (17) into

$$m_k(i', j', k') = \frac{\xi\omega(\Delta x \Delta y \Delta t)^2 \mu\mu_k}{4\pi} \sum_i^{N_x} \sum_j^{N_y} \left(S(i, j) \sum_k^{N_t} \frac{e^{-\mu k \Delta t - \mu_k \rho_{i',j',k',i,j,k}}}{\rho_{i',j',k',i,j,k}^2} \right) \qquad (19)$$

From Equation (16), we know that $\rho_{i',j',k',i,j,k}$ is only a function of $(i'-i, j'-j, k'-k)$.

Then, the number distribution of reabsorbed characteristic x-ray quanta by a sub-layer of

phosphor with index k' can be expressed as a convolution as shown by Equation (20).

$$m_k(k') = \sum_i^{N_x} \sum_j^{N_y} S(i, j) W_{blur}(i'-i, j'-j, k') = S * W(k') \qquad (20)$$

where $m_k(k')$ is the number distribution of reabsorbed K-characteristic x-ray quanta in

sub-layer k', $W(i'-i, j'-j, k')$ is the convolution kernel and it is the characteristic x-ray

re-absorption probability function and defined as

$$W(i'-i, j'-j, k') = \frac{\xi\omega(\Delta x \Delta y \Delta t)^2 \mu\mu_k}{4\pi} \sum_k^{N_k} \frac{e^{-\mu k \Delta t - \mu_k \rho_{i',j',k',i,j,k}}}{\rho_{i',j',k',i,j,k}^2} \quad \text{when } \rho_{i',j',k',i,j,k} \neq 0$$

$$W = 0 \quad \text{when } \rho_{i',j',k',i,j,k} = 0 \qquad \text{or}$$

$$W(i,j,k') = \frac{\xi\omega(\Delta x \Delta y \Delta t)^2 \mu\mu_k}{4\pi} \sum_{k}^{N_k} \frac{e^{-\mu_k \Delta t - \mu_k \rho_{i,j,k}}}{\rho_{i,j,k}^2} \quad \text{when } \rho_{i',j',k',i,j,k} \neq 0 \quad (21)$$

$$W(0,0,0) = 0$$

From Section **3**, we know that the reabsorbed characteristic x-ray quanta have different imaging performance depending on the relative position of the re-absorption site to the creation site of the reabsorbed characteristic x-ray quanta. The elements of convolution kernel $W(i,j,k')$ with $i \neq 0$ or $j \neq 0$ are related to the characteristic x-ray quanta created in the domain A of **Figure 4**. We can define these elements as a characteristic blurring probability function.

$$W_{blurring}(k') = W(i,j,k') \quad \text{when } i \neq 0 \text{ or } j \neq 0 \qquad (22)$$

The elements of convolution kernel $W(0,0,k')$ are related to the characteristic x-ray quanta created in domain B of **Figure 4**; we can define these elements as characteristic enhancing probability factors.

$$W_{enhancing}(k') = W(0,0,k') \qquad (23)$$

Substitute i with 0 and j with 0 in Equation (16) and Equation (21), we can get

$$W_{enhance}(k') = \xi\omega(\Delta x \Delta y)^2 \frac{\mu\mu_k}{4\pi} \sum_{k}^{N_k} \frac{e^{-\mu_k \Delta t} e^{-\mu_k |k'-k|\Delta t}}{(k'-k)^2} \qquad (24)$$

With Equation (22) and Equation (23), we have

$$W(k') = W_{blurring}(k') + W_{enhancing}(k') \qquad (25)$$

According to Equation (21), the characteristic x-ray re-absorption probability function is decided by the linear attenuation coefficient of the primary input x rays, the linear attenuation coefficient of the characteristic x rays, the spatial resolution of digital images,

and the number of sub-layers that the whole phosphor layer is conceptually divided. To a given image detector or intensifying screen, the characteristic x-ray re-absorption probability function of its phosphor layer can be calculated using Equation (25) for every sub-layer whenever the pixel size and sub-layer thickness are confirmed.

Theoretically, the convolution of Equation (20) should overlap the whole phosphor voxel set and the element number of characteristic x-ray re-absorption probability function of every sub-layer should be as same as the pixel number of the image. This will require not only a lot of time to compute the characteristic x-ray re-absorption probability function, but also much more time to do the convolution for every sub-layer when calculating the number distribution of characteristic x-ray quanta reabsorbed, especially if the image has many pixels and the phosphor layer of the image detectors or intensifying screen is conceptually divided into many very thin sub-layers. However, as characteristic x-ray quanta are continuously removed from the beams when traveling inside the phosphor layer, the fluence intensity of the characteristic x rays created inside the phosphor layer decays exponentially. Then, the probability that the characteristic x-ray quanta are reabsorbed by the voxels relatively far from the creating sites drops exponentially. **Table 1** lists the distances that the K-characteristic x rays can travel inside the phosphor layer before the intensity of fluence is attenuated to 1%, 5%, and 10% of the original intensity inside Gadolinium Oxysulfide and Cesium Iodide. The distance values in **Table 1** are calculated using the attenuation coefficient of the x rays at K-edge energies of the phosphor materials. If we ignore the minor contribution of the characteristic x rays that are created relatively far from the observed voxel, the

Table 2 Cut-window size to calculate the convolution of Equation (20)

Phosphor Materials	Pixel size $50 \times 50 \mu m^2$			Pixel size $17 \times 17 \mu m^2$		
	Including 99% of Characteristic x quanta	Including 95% of Characteristic x quanta	Including 90% of Characteristic x quanta	Including 99% of Characteristic x quanta	Including 95% of Characteristic x quanta	Including 90% of Characteristic x quanta
Gd_2O_2S	40	26	20	113	74	56
CsI	30	20	15	84	55	43

5 Quantitatively evaluate the effect of the reabsorbed characteristic x rays on imaging performance

Using Equation (20) and Equation (21), we can simulate the characteristic x-ray re-absorption process inside a phosphor layer and quantitatively evaluate the affect of characteristic x-ray re-absorption to the image performance of an image detector.

a) Calculate the number of reabsorbed characteristic x-ray quanta blurring the image.

We know that some reabsorbed characteristic x-ray quanta do not contain any image information and only blur the image and some reabsorbed characteristic x-ray quanta carry image information and enhance the primary input. A necessary step to calculate the number of reabsorbed characteristic x-ray quanta blurring the image by every phosphor voxel is to calculate the convolution kernel of Equation (22), the characteristic x-ray blurring probability function $W_{blurring}(k')$ for every sub-layer of the phosphor material according to the pixel size and the selected accuracy. Using Equation (21) and Equation (22), $W_{blurring}(i, j, k')$ can be calculated as a three dimensional table. **Figure 7** and **Figure 8** are two plots of the characteristic x-ray blurring probability function $W_{blur}(i, j, k')$ for

the first sub-layer of phosphor (the sub-layer is mostly close to the incident interface of the phosphor layer.) These two plots are the calculation results for a Cesium Iodide phosphor layer [17]. The total thickness of the Cesium Iodide layer is assumed as 85 μm.

When doing the calculation, the whole Cesium Iodine layer is conceptually divided into 40 sub-layers and all sub-layers have the same thickness, 2.125 μm. The image pixel size is assumed as $17 \times 17 \mu m^2$ so that the size of every Cesium Iodide voxel is $dx = 17$ μm, $dy = 17$ μm, and $dt = 2.125$ μm. The accuracy of calculation is set 95%, which includes 95% characteristic x-ray quanta created in calculation. Then, according to **Table 2,** the size of the cut-off window in **Figure 6** is 55 and $W_{blur}(i, j, k)$ is a $40 \times 110 \times 110$ table. The energy of incident x rays is assumed as 53 keV. At this energy, the linear attenuation coefficient of Cesium Iodide is $\mu = 51.34$ cm^{-1}. The K-edge energy of Cesium Iodide is 36.0/33.2 keV [1]. The attenuation coefficient at this energy is $\mu_k = 32.2$ cm^{-1}. The probability that an interacting x ray undergoes a K-shell interaction, ξ, is set as 0.85 and the fluorescent yield of K-shell photoelectric interactions, ω, is set as 0.93 according to [13]. **Figure 7** is the contour of the characteristic blurring probability function of the first sub-layer. **Figure 8** is the relative distribution of the characteristic blurring probability function of the first sub-layer. The two plots show that most of the reabsorbed characteristic x-ray quanta blurring the image are from the voxels that are close to the observed voxel. This is because the inverse square law shown by Equation (21). The intensity of the characteristic x rays becomes smaller when the observed voxel is farther from the creation site of the characteristic quanta. Equation (21) also shows the probability of re-absorption is proportional to the square of the voxel volume. Since the

voxel volume in our calculation is only $614.125 \, \mu m^3$, the absolute values of the

characteristic x-ray blurring probability function, which have unit mm^2, are relatively

small as shown by **Figure 7**.

b) Calculate the number of reabsorbed characteristic x-ray quanta enhancing the primary x-ray input.

Figure 9 is the plot of the characteristic x-ray enhancing probability factor vs. the

sub-layer index. These characteristic x-ray enhancing probability factors are calculated

with Equation (24) using the same parameters as used when calculating the characteristic

x-ray blurring probability functions. In **Figure 9**, the deeper the sub-layer is, the bigger

the index is. The sub-layer with the input interface of the phosphor layer has an index 0

and the bottom sub-layer has an index 39. The value of characteristic x-ray enhancing

probability factor is not very big because this value is proportional to the square of pixel

area.

From **Figure 9**, we can see that there is a build-up stage in characteristic x-ray

enhancing probability factor. The first sub-layer has smaller characteristic x-ray

enhancing probability factor. It increases with the sub-layer index (deeper in the

phosphor layer). After arriving at a peak value, the characteristic x-ray enhancing

probability factor decreases with sub-layer index. This is because the first sub-layer can

only reabsorb characteristic x-ray quanta created beneath it. However, the sub-layer

deeper in the phosphor layer can reabsorb the characteristic x-ray quanta created both

above it and below it, which makes the characteristic x-ray enhancing probability factor

increases. Because of the exponential factor in Equation (24), the characteristic x-ray

factor decreases as the sub-layer is far from the input interface of the phosphor layer. So,

after the peak point, as shown by **Figure 9**, the characteristic x-ray enhancing probability

factor decreases with depth. The characteristic x-ray factor drops quickly when the sub-

layers are close to the bottom of the phosphor layer since the voxels on these sub-layers

can only reabsorb the characteristic x-ray quanta created above them.

c) Calculate the variation in modulation transfer function caused by characteristic

x-ray re-absorption by numerical simulation

One way to research the effect of the characteristic x-ray re-absorption on the imaging

performance is to analyze the influence of the characteristic x-ray re-absorption to the

modulation transfer function of an image detectors or intensifying screen [18-22]. Using

the calculated characteristic x-ray blurring probability function and enhancing probability

factor, we can simulate the characteristic x-ray re-absorption process with Monte Carlo

technique. With the simulation output, we can calculate the modulation transfer function

of the image detector or intensifying screen. We did this simulation in following steps

referring to Cunningham's cascaded linear system analysis approach [23-25].

Step 1 Building an x-ray image input.

As we know, to obtain the modulation transfer function of an image detector, we

need a point x-ray image input to the image detecting system. We used Equation (26) as

our image input. This is an ideal point input because there is no x-ray quantum to all

other pixels except the central pixel. The x-ray input is assumed monochromic and at

energy 53 keV.

$$S(i, j) = \begin{cases} 1525 \text{ x - ray quanta} & \text{when } i = 127, \text{ and } j = 127 \\ 0 & \text{else} \end{cases} \quad (26)$$

where i and j are pixel indices of the image. We simulated an image detector that has

256 pixels in width and 256 pixels in height. The pixel size of the image is

$17 \times 17 \ \mu m^2$ so that the input fluence at the center of the image has a pulse of 5.3×10^6

$quanta / mm^2$

Step 2 Calculating the numbers of reabsorbed characteristic x-ray quanta blurring the image and enhancing the primary input.

This calculation can be done for every pixel using the convolution model, Equation (20) to (24), with the pre-calculated character x-ray blurring probability function and enhancing probability factor. Through this calculation, we obtained the number distributions of reabsorbed characteristic x-ray quanta blurring the image and enhancing the primary x-ray input for every sub-layer. **Figure 10** plots the accumulated number distribution of reabsorbed characteristic x-ray quanta blurring the image under the ideal point input in order to show that the pixels close to the central pixel are blurred by reabsorbing the characteristic x-ray quanta created in the voxels bellow the central pixel. In fact, the re-absorption takes place in every sub-layer so that the re-absorbed characteristic x-ray quanta have different effect on the final output image because the visible light photons produced from these reabsorbed characteristic x-ray quanta have different diffusion and absorption. In the following steps, we simulate the visible light photon production, absorption, and diffusion sub-layer by sub-layer.

Table 3 lists the accumulated number of the reabsorbed characteristic x-ray quanta blurring the image for the image pixels close to the image center where the primary input x-ray fluence pulse is. One problem is that the Monte Carlo simulation outputs are real numbers as shown in **Table 3**. Here, the decimal part can be explained as the probability of another characteristic x-ray quantum might be absorbed by the observed voxel. For example, the pixel near the center pixel has a number 3.668365. This can be understood

as that the phosphor voxels bellow this pixel reabsorbs 3 characteristic x-ray quanta.

Besides, there might be the fourth characteristic x-ray quantum reabsorbed there. The

possibility that the voxels bellow this pixel reabsorbs the fourth characteristic x-ray

quantum is 0.668365.

From **Table 3**, we can see that the pixels close to central pixel will have some image

output though there is no primary x-ray input to these pixels. The characteristic x-ray re-

absorption is equivalent to extra x-ray input sources to the phosphor layer of an image

detector or intensifying screen. After adding reabsorbed characteristic x-ray quanta from

the Monte Carlo simulation, every sub-layer of the phosphor layer gets three sources of

x-ray inputs, the primary x-ray input, the blurring x-ray input that consists of reabsorbed

characteristic x-ray quanta blurring the image, and the enhancing x-ray input that consists

of reabsorbed characteristic x-ray quanta enhancing the primary x-ray input at central

pixel. All of these three types of x-ray inputs may generate visible light and contribute to

the image output.

Step 3, Simulate the conversion process from x-ray quanta to visible light photons

inside the phosphor layers.

Table 3 The number distribution of reabsorbed characteristic x-ray quanta blurring the
image under the ideal point x-ray input.

0.344182	0.470862	0.600216	0.660068	0.600216	0.470862	0.344182
0.470862	0.732893	1.094941	1.313550	1.094941	0.732893	0.470862
0.600216	1.094941	2.240517	3.668365	2.240517	1.094941	0.600216
0.660068	1.313550	3.668365	**0.000000**	3.668365	1.313550	0.660068
0.600216	1.094941	2.240517	3.668365	2.240517	1.094941	0.600216
0.470862	0.732893	1.094941	1.313550	1.094941	0.732893	0.470862
0.344182	0.470862	0.600216	0.660068	0.600216	0.470862	0.344182

The numbers listed are accumulated reabsorbed characteristic x-ray quanta from all sub-layers. The center
of the table is the center of the image where the input x-ray pulse is. The phosphor material is Cesium
Iodide. The point input is 1525 x-ray quanta.

We use 0.15 as the conversion efficiency and 2.4 eV as the energy of a visible light

photon. Then, the conversion from x-ray quanta to visible light photons can be simulated

by

$$n_p = 0.15 \frac{E_x}{2.4} n_x \qquad (27)$$

where n_p is the number of visible light photons converted from x-ray quanta; n_x is the

number of x-ray quanta; E_x is the energy of an x-ray quantum. In our simulation, E_x is 53

keV for primary x-ray input and 34.5 keV (average of 36/33 keV) for characteristic

blurring input or enhancing input.

Step 4 Simulate the diffusion and absorption of the visible light photons inside the

phosphor layer.

The diffusion and absorption of the visible light photons inside the phosphor layer

can be simulated by Boltzmann equation [26-30]. We used the solution of Boltzman

equation in spatial frequency space, as shown by Equation (28).

$$\varphi_{u,v}(u,v,t) = \frac{\tau \rho_1 [(\omega + \tau \rho_0)e^{\alpha t} + (\omega - \tau \rho_0)e^{-\alpha t}]}{(\omega + \tau \rho_0)(\omega + \tau \rho_1)e^{\omega T} - (\omega - \tau \rho_0)(\omega - \tau \rho_1)e^{-\omega T}} \qquad (28)$$

where τ is the inverse relaxation length that describes the probability of optical

absorption occurring; ω is related to spatial frequency and $\omega^2 = \sigma^2 + 4\pi(u^2 + v^2)$ where

σ is the reciprocal diffusion length and characterizes optical scattering; u is the spatial

frequency in horizontal direction and v is the spatial frequency in vertical direction; t is

the depth of the sub-layer; T is the thickness of the phosphor layer of an image detector or

intensifying screen; $\rho_i = \frac{1 - r_i}{1 + r_i}$ where r_i is the reflectivity of the boundary of the screen;

($i = 0$) represents the interface closest to the x-ray source of the screen and ($i = 1$)

represents the output interface. To use Equation (28), we first did a Fourier

transformation to the visible light photon distribution of a sub-layer, obtained in the

conversion process from x-ray quanta to visible light photons. Then, we used this Fourier

transformation to multiply $\varphi_{u,v}(u,v,t)$ of the Equation (28). Finally, we did an inverse

Fourier transformation to get the visible light image output.

Our simulation flow is shown by **Figure 11**. We first pickup a sub-layer and

calculate the number distribution of absorbed primary input x-ray quanta. Based on the

pre-calculated characteristic x-ray blurring probability and enhancing probability, we

calculate the number distribution of the reabsorbed characteristic x-ray quanta. After this

computation, we simulate the visible light photon production, absorption, and diffusion of

the sub-layer and get the image output of this sub-layer. Then, we pickup another sub-

layer and do the same calculation and simulation again until we get the image output of

every sub-layer. Finally, we add the image output of every sub-layer together to obtain

the image output of the whole phosphor layer of the image detector or intensifying screen.

By the simulation processes above, we obtained a simulated image output of the ideal

point x-ray input image from a Cesium Iodide layer. According to the definition of

modulation transfer function, we can get the modulation transfer function of the Cesium

Iodide layer by doing Fourier Transformation to the simulated image output and

normalizing the Fourier Transformation output. **Figure 12** shows the modulation transfer

functions calculated for the Cesium Iodide layer with thickness $85\,\mu m$ and pixel

size $17 \times 17 \mu m^2$. The dashed curve in **Figure 12** is the modulation transfer function

including the characteristic x-ray re-absorption. The solid curve is the modulation transfer

function ignoring the characteristic x-ray re-absorption. From this comparison, we can

see that the spatial resolution of the image detector or intensifying screen is reduced by the characteristic x-ray re-absorption. The value of modulation transfer function is reduced from spatial frequency 0.1 mm^{-1} to 8 mm^{-1}. The biggest reduction is about 10%, which is same as the measured variation of modulation transfer function caused by characteristic x-ray re-absorption [6].

6. Summary

A convolution model is built to simulate the characteristic x-ray re-absorption based on analyzing the physics process of characteristic x-ray production and transfer inside a phosphor layer. The convolution kernel can be pre-calculated based on the physical properties of the phosphor material, the image pixel size, and the selected computation accuracy. According to the effect on the imaging performance, the reabsorbed characteristic x-ray quanta inside a phosphor layer can be separated into two types: the reabsorbed characteristic x-ray quanta blurring images and the reabsorbed characteristic x-ray quanta enhancing primary x-ray input. The convolution kernel can be expressed as a summation of the characteristic x-ray blurring probability function and the characteristic x-ray enhancing probability factor. Using the characteristic x-ray blurring probability function, we can calculate the number distribution of reabsorbed characteristic x-ray quanta blurring images. Using the characteristic x-ray enhancing probability factor, we can calculate the number distribution of reabsorbed characteristic x-ray enhancing primary x-ray input. With this convolution model, we were able to simulate the characteristic re-absorption process inside a phosphor layer of an image detector or intensifying screen by Monte Carlo technique. The output of the simulation can be used as two extra equivalent x-ray inputs, blurring characteristic x-ray input and

enhancing characteristic x-ray input, to every sub-layer of the phosphor layer inside an image detector. By generating simulated image under an ideal point input, we calculated the modulation transfer function of the image detector with characteristic x-ray re-absorption. The simulation to a Cesium Iodide layer with pixel size 17x17 μm^2 shows that the characteristic x-ray re-absorption reduces the spatial resolution of the image detector. The maximum reduction to the modulation transfer function of the image detector caused by characteristic x-ray re-absorption can as large as10%, which is in the same range as the measurement. This 3D characteristic re-absorption model can be used to simulate the imaging process of a phosphor layer and create various simulated x-ray images.

7. Acknowledgement

Reference:

[1] J. A. Rowlands, "Flat Panel Detectors for Digital Radiography," Handbook of Medical Imaging Volume 1. Physics and Psychophysics, edited by J. Beutel, H. L. Kundel, and R. L. V. Metter, SPIE Press, Bellingham, Washington, 234-253 (2000)

[2]G. Lubberts, "Random noise produced by x-ray fluorescent screens," J. Opt. Soc. Am. 58, 1475-1483 (1968)

[3]Robert K. Swank, "Absorption and noise in x-ray phosphors," J. Appl. Phys., 44, 4199-4203 (1973)   .

[4]R. Nishikawa and M. J. Yaffe, "Effects of finite phosphor thickness on detective quantum efficiency," Med. Phys. 16, 773-780 (1989)

[5]C. J. Vyborny, L. N. Loo, and K. Doi, "Relative efficiencies of energy to photographic density conversions in typical screen-film systems," Radiology, 1980, 136, 465-471

[6]B.A. Arnold and B.E. Bjarngard, "The effect of phosphor K x-rays on the MTF of rare-earth screens," Med. Phys. 6, 500-503 (1979)

[7]W. Zhao, W. G. Ji, A. Debrie, and J. A. Rowlands, "Imaging performance of amorphous selenium based flat-panel detectors for digital mammography: Characterization of a small area prototype detector," Med. Phys. 30, 254-263 (2003)

[8]H. P. Chan and K. Doi, "Studies of x-ray energy absorption and quantum noise properties of x-ray screens by use of Monte Carlo simulation", Med. Phys.11, 37-46 (1984)

[9]H. P. Chan and K. Doi, "Energy and angular dependence of x-ray absorption and its effect on radiographic response in screen-film systems," Phys. Med. Biol. 28, 565-579 (1983)

[10]C. S. Chen, K. Doi, C. Vyborny, H. P. Chan, and G. Holje, "Monte Carlo simulation studies of detectors used in the measurement of diagnostic x-ray spectra," Med. Phys. 7, 627-635 (1980)

[11]Y. Kodera, K. Doi, and H. P. Chan, "Absolute speeds of screen-film systems and their absorbed-energy constants," Radiology, 151, 229-236 (1984)

[12]J. M. Boone, J. A. Seibert, J. M. Sabol, and M. Tecotzky, "A Monte Carlo Study of x-ray fluorescence in x-ray detectors," Med. Phys. 26, 905-916 (1999)

[13]C. E. Metz and C. J. Vybnorny, "Wiener spectral effects of spatial correlation between the sites of characteristic x-ray emission and re-absorption in radiographic screen-film systems," Phys. Med. Biol. 28, 547-564 (1983)

[14]W. Hillen, W. Eckenbach, P.Quadflieg, and T. Zaengel, "Signal-to-noise performance in cesium iodide x-ray fluorescent screens," Proc. SPIE1443, 120-131 (1991)

[15]W. Zhao, W. G. Ji, and J. A. Rowlands, " Effects of characteristic x rays on the noise power spectra and detective quantum efficiency of photoconductive x-ray detectors," Med. Phys. 28, 2039-2049 (2001)

[16]K. Binder and D. Stuffer, "A simple introduction to Monte Carlo simulation and some specialized topics," Application of the Monte Carlo Method in Statistical Physics, second edition, edited by K. Binder, Springer-Verlag, 1-33 (1987)

[17]J. A. Rowlands and K. W. Taylor, "Absorption and noise in cesium iodide x-ray image intensifiers," Med. Phys. 10, 786-795 (1983)

[18]K. Rossmann, "Measurement of the Modulation Transfer Function of Radiographic Systems Containing Fluorescent Screens," Phys. Med. Biol. 9, 551-557 (1964)

[19]J. D. Gaskill, "The Spatial Frequency spectrum," A Means for Studying the Quality of Radiographic Imaging System," Radiology, 90, 1-13 (1968)

[20]C.E. Metz and K. Doi, "Transfer Function Analysis of Radiographic Imaging Systems," Phys. Med. Biol. 24, 1079-1106 (1979)

[21]J. T. Dobbins III, "Image Quality metrics for digital systems," Handbook of Medical Imaging Physics and Psychophysics, edited by J. Beutel, H. L. Kundel, and R. L. V. Metter, SPI E press, Bellingham, WA, 2000), pp. 161-222

[22]H. Fuita, D. Tsai, T. Itoh, K. Doi, J. Morishita, K. Ueda, and A. Ohtsuka, "A simple method for determining the modulation transfer function in digital radiography," IEEE Trans. Med. Imaging 11, 34-39 (1992).

[23]I. A. Cunningham and R. Shaw, "Signal-to-Noise optimization of medical imaging system," J. Opt. Soc. Am. A 16, 621-632 (1999).

[24]I. A. Cunningham, "Linear-systems modeling of parallel cascaded stochastic processes: The NPS of radiographic screens with re-absorption of characteristic X radiation," Proc. SPIE 3336, 220-230 (1998).

[25]J. Yao and I. A. Cunningham, "Parallel cascades: New ways to describe noise transfer in medical imaging systems," Med. Phys. 28, 2020-2038 (2001)

[26]R. M. Nishikawa and M. J. Yaffe, "Effect of various noise sources on the detective quantum efficiency of phosphor screens," Medical Physics, 17, No. 5, 887-893 (1990)

[27]R. M. Nishikawa and M. J. Yaffe, "Model of the spatial-frequency-dependent detective quantum efficiency of phosphor screens," Medical Physics, 17, No. 5, 894-904 (1990)

[28]R. M. Nishikawa and M. J. Yaffe, "Modeling of the spatial frequency dependent detective quantum efficiency of x-ray image receptors," Proc. SPIE 914, 128-138 (1988)

[29]R. K. Swank, "Calculation of Modulation Transfer Functions of X-Ray Fluorescent Screens", Applied Optics, 12, 1865-1870 (1973)

[30]Y. H. Zhang and R. M. Nishikawa, "Computer Simulation of Mammographic Imaging for Application in CAD," CARS 2004 Computer Assisted Radiology and Surgery, Edited by H.U. Lemke, M.W. Vannier, K.Inarmura, A. G. Farman, K. Doi, and J.H. C. Reiber, ELSEVIER, 890-895 (2004)
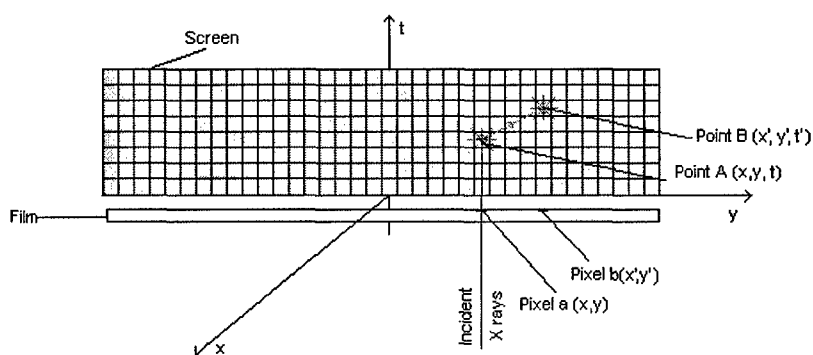
Figure 1 Schematic illustration of the generation and re-absorption of characteristic x

rays inside the phosphor layer of an image detector or intensifying screen.
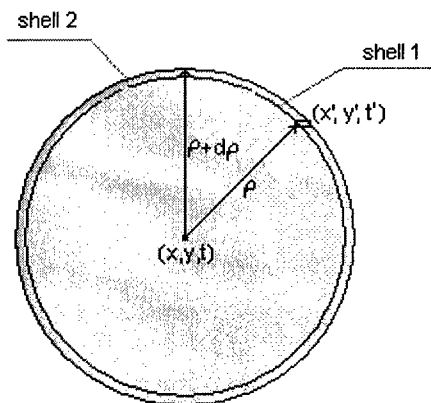
Figure 2 The characteristic x-ray quanta created in voxel centered at (x, y, t) emit isotropically.
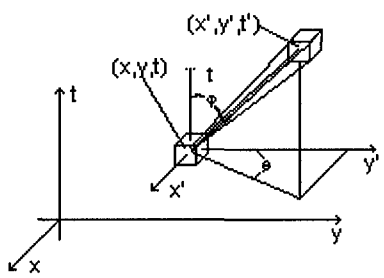
Figure 3 the relationship between the re-absorption voxel centered at (x', y', t') of the K-characteristic x-rays and the creation voxel centered at (x, y, t).
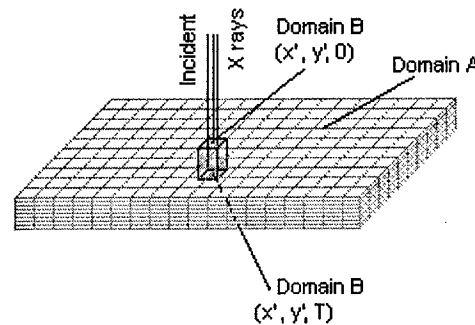
Figure 4 The whole phosphor layer is conceptually divided into multiple sub-layers with equal thickness Δt. The phosphor layer looks as a voxel set with $N_x \times N_y \times N_t$ voxels. The integration to calculate the total number of reabsorbed characteristic x rays by voxel centered at (x', y', t') blurring the image is over the whole voxel set except the voxels in the bar from the voxel centered at $(x', y', 0)$ to the voxel centered at (x', y', T).
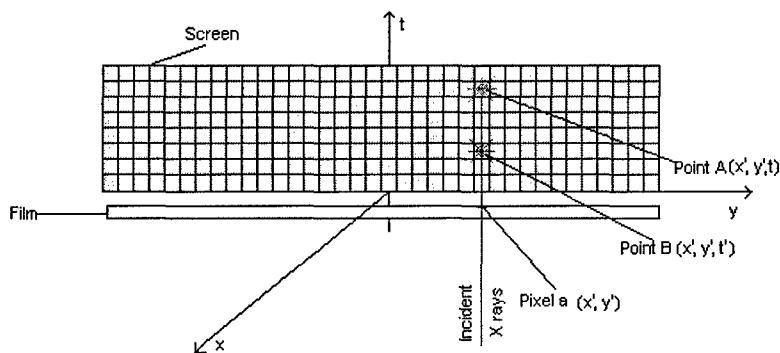
Figure 5 Schematic illustration that some of reabsorbed characteristic x-ray quanta enhance the primary x-ray input.
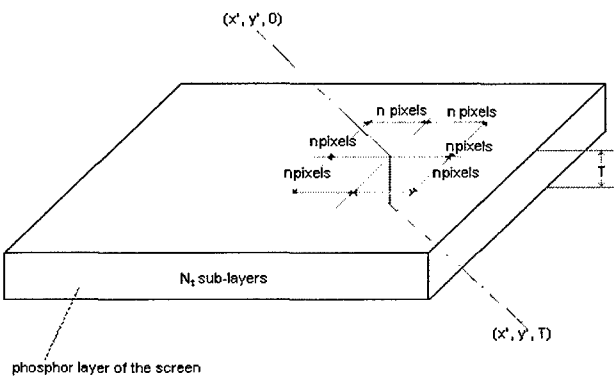
Figure 6 The computation to calculate the number of the reabsorbed characteristic x-ray quanta in a voxel inside the bar from $(x', y', 0)$ to (x', y', T) needs only to cover the space in the window. The number of total voxels involved is $4n^2 N_t$.
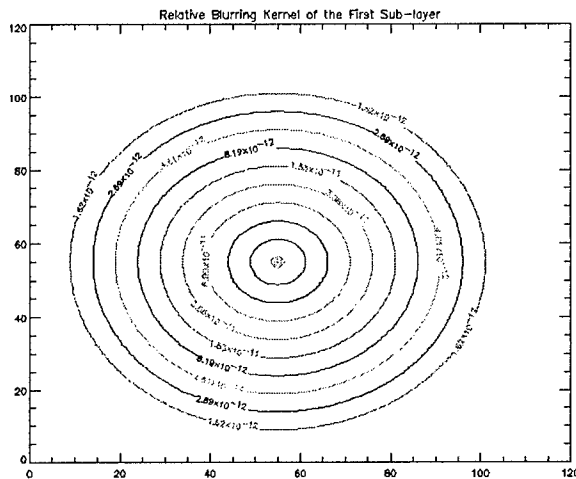
Figure 7 Contour of characteristic blurring probability function (table) on the first sub-layer of a Cesium Iodide phosphor layer. The thickness of the sub-layer is 2.125 μm. The thickness of the whole phosphor layer is 85 μm. The pixel size is 17×17 μm^2. The index should add a bias -55 when using this 2 dimensional table to do the convolution. Every sub-layer has its own table similar to this table.
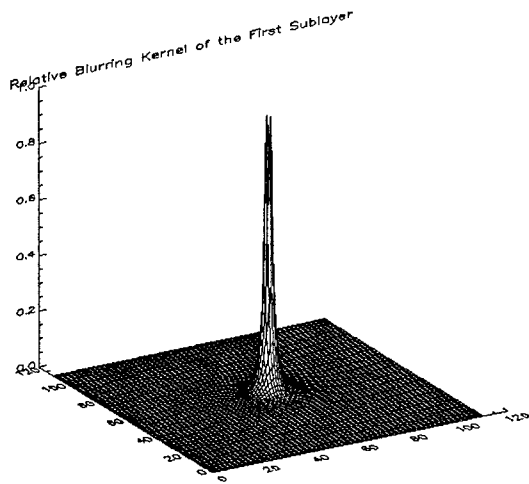
Figure 8 The relative characteristic blurring probability function of the first sub-layer in a Cesium Iodide phosphor layer. A bias -55 should be added to the index when using this 2D table. Then, the center becomes (0, 0), which is the observed voxel. The value of every element is the relative probability that a created characteristic x-ray quantum is reabsorbed by the observed voxel. The drawing shows that the characteristic x-ray quanta created in the voxels close to the observed voxel have larger probability to be reabsorbed by the observed central voxel.
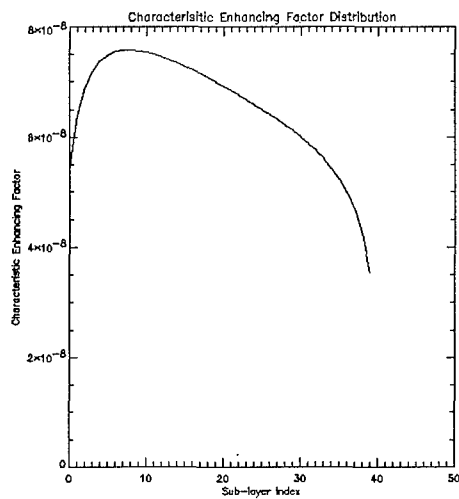
Figure 9 Characteristic x-ray enhancing probability factors of all sub-layers in a Cesium

Iodide phosphor layer. The thickness of phosphor layer is assumed as 85 μm. The whole

phosphor layer is conceptually divided into 40 sub-layers and each sub-layer is 2.125 μm

thick.
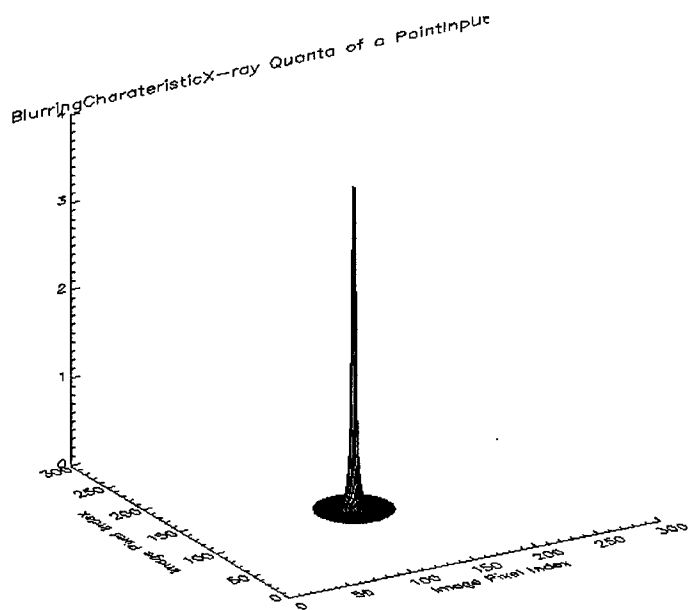
Figure 10 the number distribution of characteristic x-ray quanta blurring the image

under the ideal point image input. The distribution is obtained from Monte Carlo

simulation using Equation (20). The pixels close to the central input pulse are blurred by

the characteristic re-absorption.
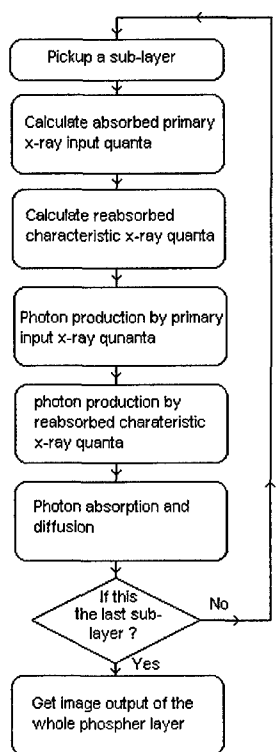
Figure 11 the flow chart to simulate the imaging process of a phosphor layer inside an

image detector or intensifying screen
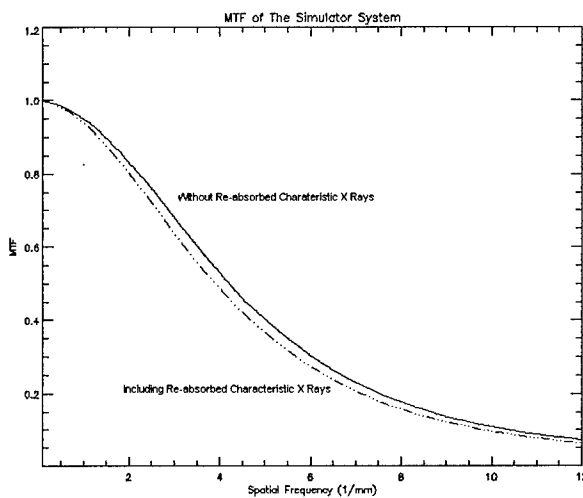
Figure 12 Modulation transfer function (MTF) calculated for a Cesium Iodide layer from simulation. The thickness of the Cesium layer is assumed $85 \, \mu m$ and pixel size $17 \times 17 \mu m^2$. The phosphor layer is conceptually divided into 40 sub-layers. The solid curve is the modulation transfer function without considering characteristic x-ray re-absorption. The dashed curve is the modulation transfer function including characteristic x-ray re-absorption. The spatial resolution of the detector is reduced by characteristic x-ray re-absorption